



Project 010 Aircraft Technology Modeling and Assessment

Georgia Institute of Technology Purdue University

Project Lead Investigators

Dimitri Mavris (P.I.)
Regents Professor
School of Aerospace Engineering
Georgia Institute of Technology
Mail Stop 0150
Atlanta, GA 30332-0150
404-894-1557
dimitri.mavris@ae.gatech.edu

William Crossley (P.I.)
Professor
School of Aeronautics and Astronautics
Purdue University
701 W. Stadium Ave
West Lafayette, IN 47907-2045
765-496-2872
crossley@purdue.edu

Jimmy Tai (co-P.I.)
Senior Research Engineer
School of Aerospace Engineering
Georgia Institute of Technology
Mail Stop 0150
Atlanta, GA 30332-0150
404-894-0197
jimmy.tai@ae.gatech.edu

Daniel DeLaurentis (co-P.I.)
Professor
School of Aeronautics and Astronautics
Purdue University
701 W. Stadium Ave
West Lafayette, IN 47907-2045
765-494-0694
ddelaure@purdue.edu

University Participants

Georgia Institute of Technology (Georgia Tech)

• P.I.s: Dr. Dimitri Mavris (P.I.), Dr. Jimmy Tai (co-P.I.) FAA Award Numbers: 13-C-AJFE-GIT-006, 13-C-AJFE-GIT-012, 13-C-AJFE-GIT-022, 13-C-AJFE-GIT-031, 13-C-AJFE-GIT-37, 13-C-AJFE-GIT-041, 13-C-AJFE-GIT-50, 13-C-AJFE-GIT-52, 13-C-AJFE-GIT-56, 13-C-AJFE-GIT-76, and 13-C-AJFE-GIT-94, 13-C-AJFE-GIT-134, and 13-C-AJFE-GIT-136









Period of Performance: September 1, 2023 to December 31, 2023

Purdue University

- P.I.s: Dr. William A. Crossley (P.I.), Dr. Daniel DeLaurentis (co-P.I.)
- FAA Award Numbers: 13-C-AJFE-PU-004, 13-C-AJFE-PU-008, 13-C-AJFE-PU-013, 13-C-AJFE-PU-018, 13-C-AJFE-PU-026, 13-C-AJFE-PU-032, 13-C-AJFE-PU-035, 13-C-AJFE-PU-044, and 13-C-AJFE-PU-047
- Period of Performance: September 1, 2022 to August 31, 2023

Project Funding Level

The project is funded by the FAA at the following levels: The funding for the last period of performance was Georgia Tech: \$200,000; Purdue University: continuing on a no-cost extension which ended during the period covered in the 2023 annual report. Cost-sharing details are below:

Georgia Tech has agreed to a total of \$200,000 in matching funds. This total includes in-kind cost-sharing from Boom Supersonics; salaries for the project director, research engineers, and graduate research assistants; and funding for computing, financial, and administrative support, including meeting arrangements. The institute has also agreed to provide tuition remission for the students, paid for by state funds.

Purdue completed their work with the performance period covered in the 2023 Annual report. They were continuing under a no cost extension. The last FAA funding to Purdue University for this project provided a total of \$225,000. Purdue provides matching support through salary support for the faculty P.I.s, as well as salary support, and tuition and fee waivers for one graduate research assistant working on this project. OAG Aviation Worldwide Limited also provided in-kind cost-sharing to the Purdue team. The total of these matching funds is \$225,000.

Investigation Team

Georgia Institute of Technology

Dimitri Mavris (P.I.), All Tasks

Jimmy Tai (co-P.I.), Tasks 1, 2, 3, 4 and 5

Jai Ahuja (research faculty; vehicle modeling technical lead), Task 1

Christian Perron (research faculty; vehicle modeling technical lead), Task 1

Chung Lee (research faculty; vehicle modeling technical lead), Task 1

Brennan Stewart (research faculty; vehicle modeling technical lead), Task 1, 4, and 5

James D. Kenny (research faculty; vehicle modeling technical lead), Task 2

Holger Pfaender (research faculty, fleet modeling technical lead), Task 3

Edan Baltman (graduate student), Task 2 and 5

Joao De Azevedo (graduate student), Task 4 and 5

Barbara Sampaio (graduate student), Task 1

Jiajie (Terry) Wen (graduate student), Task 3

Ted Vlady (graduate student), Task 2

Nikhil Iyengar (graduate student), Task 1

Zayne Roohi (graduate student), Task 2

Srikanth Tindivanam Varadharajan (graduate student), Task 2

Carter J. Tegen (graduate student), Task 2

Divya K. Kalaria (graduate student), Task 1

Madeleine E. Graham Macy (Undergrad student), Task 1

Purdue University

William Crossley (P.I.), Task 6
Daniel DeLaurentis (co-P.I.), Task 6
Muharrem Mane (research faculty), Task 6
Tien-Yueh Fung (graduate student), Task 6
Krinal Doma (Undergrad student), Task 6







Project Overview

Georgia Tech and Purdue University teams have partnered to investigate the future demand for supersonic air travel and the environmental impacts of supersonic transports (SSTs). In the context of this research, the environmental impacts include direct carbon dioxide (CO₂) emissions, noise, and fuel consumption. The research is conducted as a collaborative effort to leverage the capabilities and knowledge of the multiple entities that make up the ASCENT university partners and advisory committee. The primary objective of this research project is to support the FAA in modeling and assessing the potential future evolution of the next-generation supersonic aircraft fleet. The research in this project consists of five integrated focus areas: (a) establishing fleet assumptions and performing demand assessment (completed in 2021); (b) performing preliminary SST environmental impact prediction (completed in 2023); (c) developing approaches to model SSTs within the FAA Aviation Environmental Design Tool (completed in 2022); (d) performing vehicle and fleet assessments of potential future supersonic aircraft (completed in this report); and (e) performing physics-based modeling of SSTs and conceptual design by using the Framework for Advanced Supersonic Transport (FASST) (completed in this report).

To better understand the potential demand for supersonic air travel, the team has developed a parametric airline operating-cost model to explore the sensitivities of key vehicle, operational, and cost parameters on the required yield that an airline would need to target for ticket prices on potential new supersonic aircraft. However, the current model assumes fixed parameters for key vehicle metrics, which can be changed but do not include sensitivities to key vehicle design choices, such as vehicle size, design cruise Mach number, and maximum range. The fleet analysis work examines the implications of the physical and technical dependencies on airline operational cost. Through the vehicle performance sensitivities, such as passenger capacity and design cruise Mach number, the combined "sweet spot," i.e., the most profitable vehicle for an airline to operate, can be determined. To accomplish this goal, the existing vehicle models created in the prior year are used and supplemented with the additional vehicles proposed in this period of performance. These vehicles together serve as the foundation to create credible sensitivities regarding parameters such as vehicle size and design cruise Mach number. These sensitivities are then embedded in the airline operating-cost estimation model and used to explore the combined vehicle and airline operational space to identify the most economically feasible type of supersonic vehicle. This work is described in pervious annual reports.

In an independent complementary approach, to consider the demand and routes for supersonic aircraft, the Purdue team had developed a ticket pricing model for possible future supersonic aircraft. The model relies on the "as-offered" fares before the novel coronavirus (COVID-19) pandemic, for business-class and first-class tickets on routes expected to have passenger demand for supersonic aircraft. Through considering the number of passengers potentially demanding fares at business class or above on a city-pair route, the distance of that city-pair route, an adjustment to increase the over-water distance of the route where the aircraft can fly supersonically to allow for the shortest trip time, and the range capability of a low-fidelity modeled medium SST (55 passenger [pax]) to fly that route with the shortest trip time, the Purdue team had identified a network among 257 airports that could potentially allow for supersonic aircraft service in a network of routes with at least one end (i.e., origin or destination) in the United States. This work is described in pervious annual reports.

One major accomplishment of the project during the performance period is the provision of preliminary results for the design of a 65-pax SST designed for a mission of 4,250 nmi designed to cruise Mach 1.7. An 8-pax business jet has also been designed, which would cruise at Mach 1.4 for a design range of 4,250 nmi. The preliminary results were arrived at through computational fluid dynamics (CFD)-based vehicle shape optimization, engine cycle modeling with Numerical Propulsion System Simulation (NPSS), and noise modeling with NASA's Aircraft Noise Prediction Program (ANOPP), and mission analysis and detailed landing and takeoff (LTO) analysis incorporating a variable noise-reduction system (VNRS) by using the Flight Optimization System (FLOPS). These modeling approaches and programs were integrated into FASST, thus allowing the Georgia Tech team to generate interdependency results between fuel burn (or maximum takeoff weight) and certification cumulative noise levels (in effective perceived noise in decibels [EPNdB]). Although previous periods of performance have also produced vehicle design, these designed were created under Georgia Tech latest methodology and most up to date assumptions.

The Georgia Tech team has also performed a study of variable takeoff climb-speed requirements ($V_2 + x$) on the Mach-1.7, 65-pax SST and Mach-1.4, 8-pax SST in this performance period. Although subsonic aircraft takeoff climb speeds for certification are restricted to between $V_2 + 10$ and $V_2 + 20$, whether this constraint is appropriate for supersonic vehicles is unclear. This study's objective was to determine how for a fixed vehicle design, takeoff noise would be affected by different reference climb speeds. Georgia Tech optimized the trajectory for each target reference climb speed with various degrees of





freedom in the takeoff procedure to examine how a fully reoptimized takeoff procedure and takeoff procedures with certain fixed parameters would display different noise sensitivities to reference climb speed.

Although the Purdue team completed their work during the period of performance covered by the 2023 annual report, overview of their final period of performance is as follows. The Purdue team had pursued three subtasks as part of the fleet analysis task. During Purdue's last year, the team had created and used the performance and cost coefficient of six additional SST concepts of combinations of passenger capacity and Mach number, implemented a sustainable aviation fuel (SAF) price evolution model, and estimated the effects of SAF utilization in subsonic-only and subsonic and supersonic scenarios. With modifications to FLEET to accommodate these changes, the team has estimated the impacts on future environmental emissions when different types of SST concepts are introduced into the fleet and when SAFs are used to reduce the impact of the SST.

Milestones

The Georgia Tech team had four milestones for this year of performance:

- 1. Developed a detailed operation procedure for VNRS takeoff procedure for SST concepts
- 2. Designed and analyzed two SST configurations, (Mach 1.4 8-pax Business Jet and Mach 1.7 65-pax SST)
- 3. Conducting a study on the effects of Part 36 takeoff reference speed regulations on certification noise levels

The Purdue team completed their work during the period of performance covered in the 2023 annual report, please refer to that report for the milestones for Purdue during their final performance period

Major Accomplishments

Major accomplishments of the project during the period of performance include the analysis and multi-objective design optimization of Mach 1.7 65-pax SST and a Mach 1.4 8-pax SST. The multi-objective optimization objective was to select a design point for each configuration which minimizes fuel at the minimum acceptable noise resulting from a design space exploration the of engine cycle, thrust loading, wing loading, and take-off operational procedure parameters. The aerodynamic performance of the vehicles was obtained through CFD-based aerodynamic shape optimization of the aircraft geometry, the engine analysis was performed via a custom developed NPSS engine, the noise analysis was conducted using the NASA ANOPP software, and the mission analysis coupled with detailed LTO analysis was conducted using FLOPS. The detailed LTO analysis included consideration of a variable noise reduction system allowing for an advanced take-off procedure to mitigate noise. The Georgia Tech team used the Mach 1.7 65-pax design and the Mach 1.4 8-pax design to conduct studies on the Part 36 takeoff reference speed ($V_2 + x$) under various takeoff procedures to examine whether the current subsonic requirements might be appropriate for supersonic vehicles.

Task 1 - SST Aerodynamic Modeling

Georgia Institute of Technology

Objectives

The two primary objectives were as follows:

- Aerodynamic shape optimization of the SST outer mold line for a given cruise Mach number (for a fixed planform area and wing capture area)
- Generation of parametric drag polars for the optimized vehicle that capture aerodynamic performance across the entire flight envelope, as a function of wing planform area and inlet capture area

Research Approach

Analysis workflow

A general analysis process was developed to determine the aerodynamic performance of multiple aircraft designs. This process was then automated with Python and implemented by using Georgia Tech's high-performance computing facilities. Because the analysis workflow was automated and easily parallelizable, many designs were able to be analyzed at once. The ability to complete hundreds of aerodynamic analyses in a matter of hours enabled rapid evaluation of designs and generation of drag polars.







Starting from a set of design variables, the first step was to generate a computer-aided design (CAD) representation of the aircraft geometry. This process used the Engineering Sketch Pad, a lightweight, open-source CAD tool developed by the Massachusetts Institute of Technology (Haimes & Dannenhoffer, 2013), which allows users to easily script the generation of complex geometries and expose design parameters. Therefore, changing global parameters, such as the sweep angle or taper ratio, automatically and seamlessly scaled and repositioned the different sections of the wing. After a new geometry was defined, it was then saved to a generic CAD file (in EGADS format in the current workflow) and tessellated for later use in CFD analysis.

The outer mold line was tailored to maximize the lift/drag (L/D) ratio at the design cruise Mach number as a surrogate to minimize mission fuel burn. The optimization was divided into three stages: two initial phases focusing on the fuselage and vertical tail (VT) design, and one main stage focusing on the wing planform optimization. Both inviscid (Euler) and Reynolds-averaged Navier–Stokes (RANS) CFD analyses were used in a multi-fidelity optimization approach to decrease design time and cost. NASA's Cart3D (NASA Advanced Supercomputing Division, n.d.) was used as the inviscid solver, and Siemens' STAR-CCM+ (Siemens, n.d.) was used as the RANS solver. The following sections detail each airframe design phase.

Fuselage design

With the number of passengers set according to the requirements, the fuselage design, in terms of minimum cabin length and width requirements, is constrained by the cabin layout. Whereas slender fuselages are preferable for supersonic cruise performance, care must be taken to avoid an excessively long body, because takeoff rotation constraints necessitate longer and thus heavier landing gear. After the cabin layout is frozen (cabin layout assumed for the 65-pax aircraft shown in Figure 1), additional refinements are conducted on the fuselage nose and tail cone sections, in terms of length and cross-sectional radius, to optimize for cruise L/D. During this fuselage design process, the wing planform is frozen. A design of experiments (DoE) is developed, with the length of the nose, length of the tail, and cross-sectional radii for various stations of the fuselage as independent variables. CART3D with a single-pass viscous correction is used for the aerodynamic analysis. The results from this DoE are used to train a neural-network surrogate, which in turn is used to optimize the vehicle for cruise L/D. The resulting fuselage design is then frozen and used in the wing optimization stage.

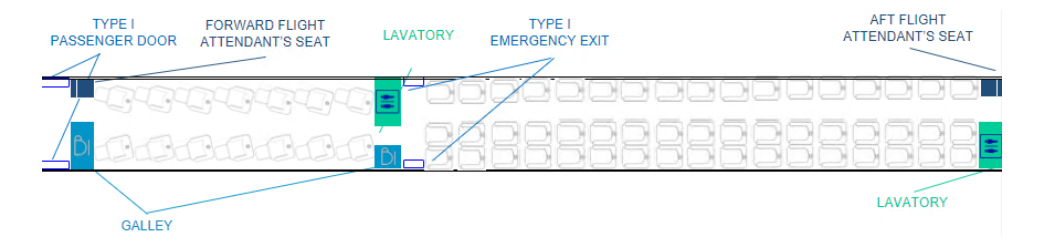


Figure 1. Cabin layout for a 65-pax aircraft.

VT design

The VT design is based primarily on two critical Federal Aviation Regulations (FAR): §25.147 for directional control under two-engine inoperative conditions and §25.237 for cross-wind requirements. Directional stability is analyzed with first-order principles and semi-empirical relations, rather than CFD. The design variables considered are wing planform area, aspect ratio, taper ratio, leading edge sweep, and thickness to chord. The goal is to find the smallest VT planform area satisfying the requirements for the furthest feasible VT location relative to the wing. A symmetric biconvex airfoil is used, with a thickness-to-chord ratio (t/c) fixed to a value that ensures an adequate cross-sectional thickness for the rudder actuators but is sufficiently small to avoid penalizing supersonic cruise performance. The rudder chord length to mean aerodynamic chord fraction is set to 0.35.

Wing planform design

Because the aerodynamic performance of the vehicle is strongly dependent on the wing planform, most of the optimization effort is focused on this component. As such, RANS CFD is used to analyze the performance of each design perturbation. The wing is defined by two sections, inboard and outboard, and five airfoil profiles. Global variables such as the taper ratio, aspect ratio, sweep, and dihedral apply to the entire wing, whereas the delta variables control the difference between the inboard and outboard sections. The wing break location variable determines the spanwise extent of the inboard section relative to the outboard, for a fixed total span. Biconvex airfoils are used to define the wing, with twist and camber being part of the design space. The maximum camber is limited to half the specified t/c ratio.







Given the dimensionality of the problem and the cost of each function call, this optimization exercise must be performed strategically. As such, a gradient-free active subspace approach is first used to reduce the dimensionality of the design space by using the less expensive inviscid CFD. Subsequently, adaptive sampling is performed in this reduced design space with RANS simulations to improve the L/D. A high-level overview of this process is shown in Figure 2. The goal of the active subspace method (Constantine et al., 2014) is to reduce the high-dimensional input space of some function to a lower-dimensional subspace, the so-called active subspace. For instance, given a function f(x), where $x \in \mathbb{R}^d$ is a high-dimensional input vector, the following approximation is made:

$$f(\mathbf{x}) \approx g(\mathbf{z}) = g(\mathbf{W}^T \mathbf{x}) \tag{1}$$

where $g(\mathbf{z})$ is an approximate predictor of f(x), and $\mathbf{W} \in \mathbb{R}^{d \times k}$ is a projection matrix that maps the inputs x to a low-dimensional representation $\mathbf{z} \in \mathbb{R}^k$, which are referred to as the active variables with k < d. That is, the active subspace method aggregates potentially many design variables into several modes that best capture the variability of the output. Consequently, the efficiency of optimization with respect to the active variables increases, because the size of the design space is exponentially reduced. Fitting a surrogate to predict the output of interest is also made easier, because the active subspace alleviates the infamous "curse of dimensionality." The main difficulty of the active subspace method is in finding the matrix \mathbf{W} that best approximates the variability of f(x). Although most dimensionality reduction methods are unsupervised, the active subspace is a supervised approach. Thus, the reduction of the input spaces is not based on the similarity between design vectors but instead is informed by the functional dependence between the input and the output spaces.

The classical active subspace approach for dimensionality reduction proposed by Constantine relies on the gradient information of the objective function, which can be challenging to obtain. Although gradient-free approaches have been proposed in the literature (Tripathy et al., 2016; Seshadri et al., 2019; Gautier et al., 2021), these methods require extensive sampling of the objective function, which can be costly in scenarios in which the objective is being evaluated by high-fidelity codes, such as RANS solvers. To counter this drawback, Mufti et al. (2022) have proposed a gradient-free multi-fidelity approach in which a lower-fidelity and relatively less expensive code, in this case Cart3D, is used to extract an approximation of the RANS active subspace. The requirement for this approach is an initial DoE that samples the design space. Each case in this DoE is evaluated in Cart3D, and the L/D is recorded. The proposed multi-fidelity approach is then applied to obtain a reduced representation of the design variables, on the basis of the lower-fidelity results. Although the inviscid L/D results from Cart3D are not as accurate as those obtained with RANS, both tend to have similar behaviors. Therefore, an active subspace computed by using inviscid results can reasonably be assumed to be a good representation of the corresponding subspace that would be obtained with RANS results. Mufti et al. have demonstrated that this assumption holds for the design of transonic airfoils and wings. Although using lower-fidelity results to compute the active subspace has drawbacks and does reduce the accuracy of the method, it also significantly decreases the cost of computing the active subspace. For the purposes of this work, this trade-off between accuracy and computational cost is considered acceptable.

After the reduced representation of the design variables is determined, the RANS optimization process begins. The objective function is maximized through an adaptive sampling approach using the efficient global optimization (EGO) method (Jones et al., 1998). To start the process, a warm-start DoE is run to train a Kriging surrogate model. The Kriging model not only provides a prediction of the objective function at non-sampled points but also provides an estimate for the model's prediction uncertainty between two sampled points. These two components are used in the EGO method to balance "exploration" versus "exploitation" of the design space. In the current context, "exploration" refers to sampling in regions where model uncertainty is high, and "exploitation" denotes sampling in regions close to the optimum. After the initial warm-start DoE and model training, a small number of candidate points are selected that maximize the "expected improvement" criterion of the objective function. These samples are then evaluated in RANS, the Kriging model is retrained, the expected improvement is recomputed, and the process repeats until a user-defined stopping condition is met. In this fashion, the aerodynamic performance of the vehicle is improved iteratively. The sample size of the warm-start DoE and the number of additional samples required depend on the dimension of the design space; consequently, the active subspace dimensionality reduction in the previous step is critical for minimizing the overall design time and cost.





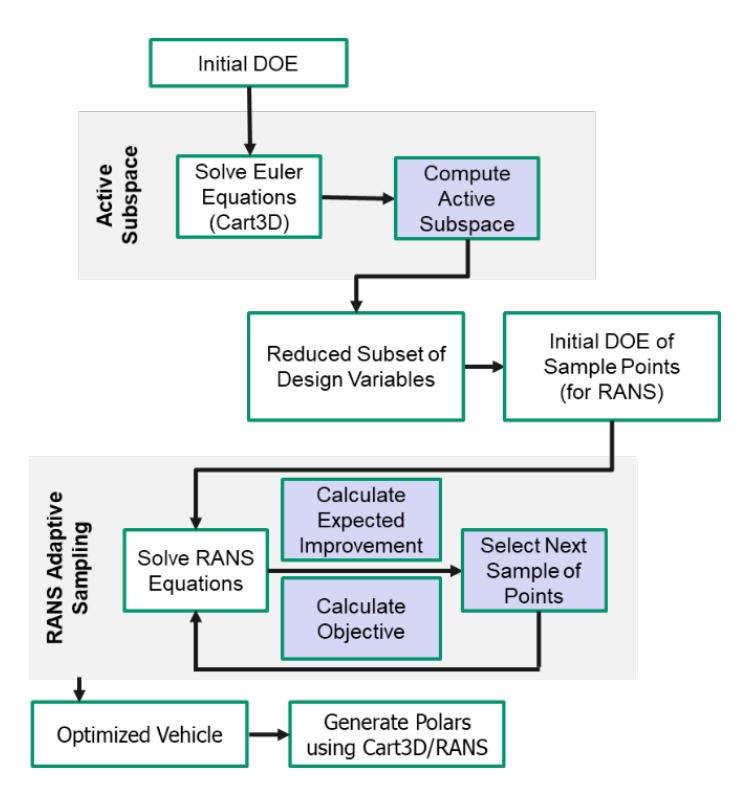


Figure 2. Aerodynamic optimization process (DOE, design of experiments; RANS, Reynolds-Averaged Navier-Stokes).

Of note, for some vehicles, the optimization process would converge on a wing design with an excessive sweep and aspect ratio. The resultant vehicle would then have a large wing weight during the system analysis, which would severely hinder mission performance, because the wing planform design is purely aerodynamic and lacks any structural consideration. To circumvent this issue, an upper limit on wing weight has been added to the adaptive sampling approach. Consequently, the EGO algorithm searches for new samples that maximize the expected improvement of the objective while having a high probability of meeting the wing weight constraint according to the process described previously (Forrester & Keane, 2009). For this purpose, the wing weight is estimated from a given planform by using the FLOPS weight equations (Wells et al., 2017). From these weight estimates, an additional Kriging model is trained, which is then used to predict the likelihood of a new design to satisfy the weight constraint.

Figure 3 shows an example of a design optimized with and without the wing weight constraint.





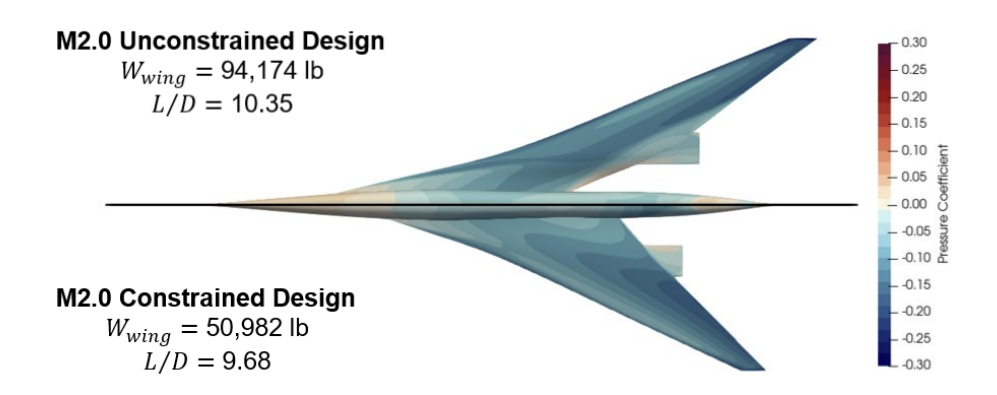


Figure 3. Comparison between an unconstrained and a wing-weight-constrained optimum (W_{wing} , wing weight; L/D, lift-to-drag ratio).

Drag polar generation for an optimized vehicle

After the vehicle with the highest cruise L/D is obtained, to enable mission analysis, drag polars for every point in the operating envelope are generated in the form of a table with Mach, altitude, lift coefficient ($C_{\rm L}$), and drag coefficient ($C_{\rm D}$) as the columns. Generating a drag polar that covers the entire envelope is quite costly to perform solely with RANS CFD. Therefore, a hybrid approach is used, as shown in Figure 4. First, the less expensive Cart3D is used to generate a set of "baseline polars" for all Mach-number and angle-of-attack combinations. Because Cart3D is an inviscid solver, altitude is not an input, because it affects only viscous forces. RANS CFD is then used to sample a subset of the low-fidelity flight conditions. In this case, 15 RANS samples are considered. The flight conditions for these RANS cases are chosen strategically to minimize the root-mean-square error of the surrogate model and the number of high-fidelity cases required to achieve such minimization. Because altitude is not a consideration for the low-fidelity CFD, values are assigned to each RANS sample to spread them out uniformly in the expected Reynolds-number range. These viscous results are then used to calibrate the inviscid polars to account for viscous effects. Hierarchical Kriging (Han & Görtz, 2012), a type of multi-fidelity surrogate model, is used. In this situation, the low-fidelity data are the numerous Cart3D results, and the high-fidelity samples are the few RANS CFD solutions.

Parametric drag polars capturing the effects of changing wing planform area and inlet capture area

Aerodynamic optimization is conducted for a fixed-wing planform area and inlet capture area. However, as part of vehicle sizing and mission analysis, both the engine size and wing planform area are allowed to scale. To account for the effects of these changes on the aerodynamic performance of the vehicle, having a set of drag polars that are a function of these design variables is desirable. This objective is efficiently achieved through a proper orthogonal decomposition (POD) reduced-order model (ROM).

A parametric ROM approximates the prediction of a function by mapping an *m*-dimensional input vector to a *d*-dimensional output vector. In contrast to a conventional surrogate model, the quantity being predicted is a high-dimensional vector. The development of parametric drag polars at a high level is illustrated in Figure 5 and largely follows previously described work (Lee et al., 2011) using a similar approach for a parametric engine deck. The main steps are as follows. First, a DoE is created to sample the design space spanned by the wing planform area and inlet capture area. Ten samples are defined with unique combinations of the two design variables. The nacelle length is correlated with the inlet capture area and is thus a fallout. A multi-fidelity mission drag polar is generated for each of sample in the DoE through the process outlined in the preceding section. These drag polars are then used as observations to train the ROM. After the modes and coefficients for the POD model are obtained, a radial basis function is used as the interpolating mechanism for the POD coefficients, such that drag polars can be predicted at previously unseen values of the design variables.





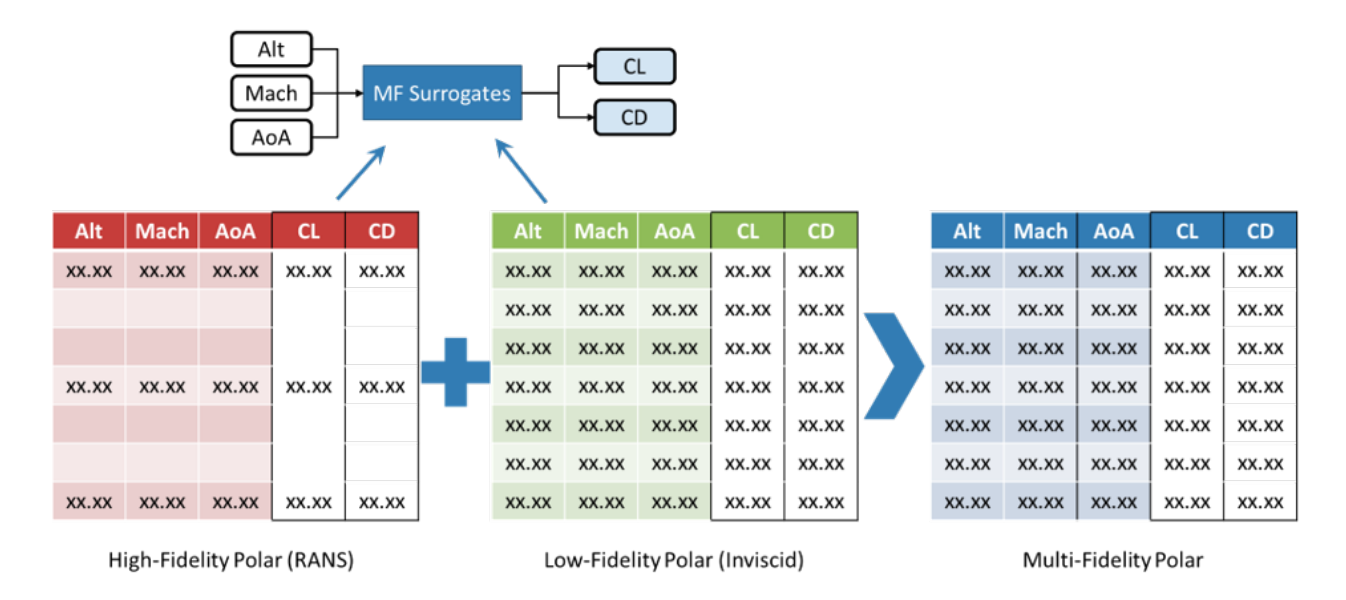


Figure 4. Schematic of the multi-fidelity drag polar generation process (Alt, altitude; AoA, angle of attack; MF, multi-fidelity; C_L , lift coefficient; C_D , drag coefficient).

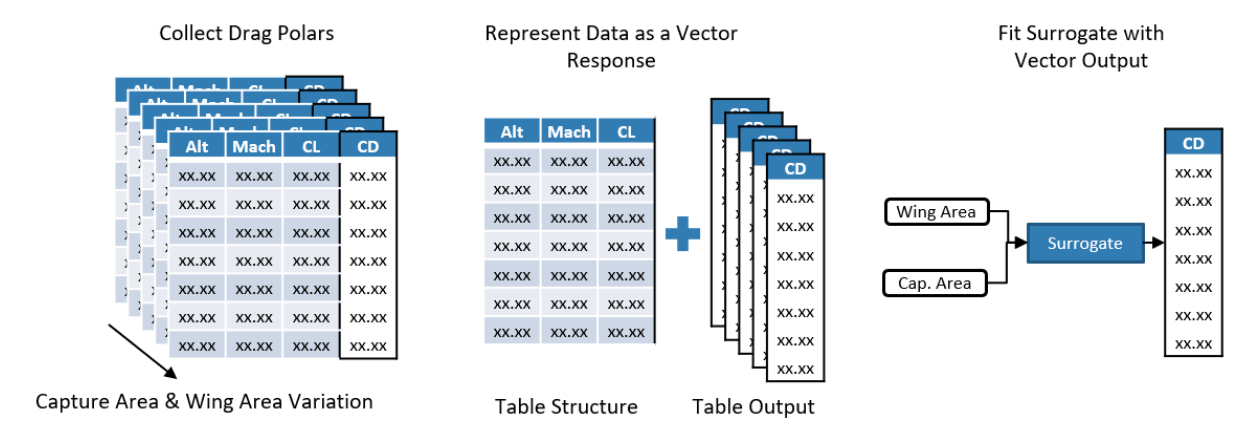


Figure 5. Schematic of the construction of the parametric drag polars (Alt, altitude; C_L , lift coefficient; C_D , drag coefficient).

Results

65-pax, Mach-1.7 Design

The fuselage and VT used for this aircraft remained fixed during the design process. The present aircraft shared the same fuselage and VT used by the 65-pax vehicles described in the 2022 report. The vehicle wing design was performed to obtain the optimum geometry for this cruise Mach number. The wing design is described below.

For this study, the planform area of the wing is fixed at $5,125 \, \mathrm{ft}^2$. In total, there are 18 geometric variables (Table 1) with angle of attack being the 19th design variable. One hundred warm-start cases are executed to sample the design space initially, followed by an additional 100 adaptive samples. The adaptive sampling is stopped when the expected improvement in L/D is on the order of 0.01. Figure 6 shows the distribution of L/D over the warm-start and adaptive samples. As depicted in this figure, the majority of the adaptive sampling cases (blue and purple) have L/D values between 9 and 10 at cruise. Some adaptive samples with lower L/D (between 5 and 9) correspond to early points in the adaptive sampling; i.e., during the "exploration phase" of the optimization.







Table 1. Wing design variables and bounds.

Parameter	Lower Bound	Upper Bound	Parameter	Lower Bound	Upper Bound
Overall taper	0.1	0.3	Delta c/4 sweep break [deg]	-20	0
Overall AR	2.25	4	Section 1 (twist, max camber)	[0, 0%]	[1.5, 0.5(t/c)]
Overall c/4 sweep [deg]	40	60	Section 2 (twist, max camber)	[-5, 0%]	[5, 0.5(t/c)]
Overall dihedral [deg]	-5	5	Section 3 (twist, max camber)	[-5, 0%]	[5, 0.5(t/c)]
Delta taper break	0	0.3	Section 4 (twist, max camber)	[-5, 0%]	[5, 0.5(t/c)]
Delta dihedral break [deg]	-5	5	Section 5 (twist, max camber)	[-5, 0%]	[5, 0.5(t/c)]
Wing break location	0.3	0.6			

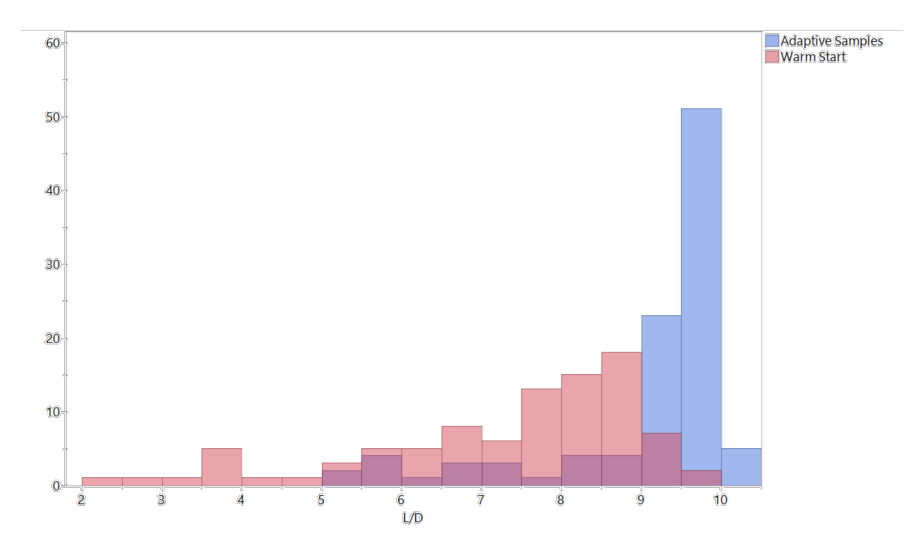


Figure 6. Distribution of lift to drag (L/D) over warm-start and adaptive sampling.

Figure 7 shows a comparison of baseline and optimized wing planforms with the design variable values compared in Table 2. The major differences in the optimized vehicle relative to the baseline are the larger sweep, an inboard shift in the wing break location, and a change in the twist distribution and camber of the wing. The highest L/D for this vehicle at cruise is 10.16 for a C_L of 0.156, which is a 9.25% improvement over the baseline vehicle peak L/D, which occurs at a C_L of 0.146.

Table 2. Comparison of baseline and optimized wing design variables.

Parameter	Baseline	Optimized	Parameter	Baseline	Optimized
Overall taper	0.1	0.109	Delta dihedral break [deg]	0	0.08
Overall AR	2.5	2.519	Section 1 (twist, max camber)	[0, 0%]	[0.77, 0.92%]
Overall c/4 sweep [deg]	52.5	61.65	Section 2 (twist, max camber)	[0, 0%]	[0.93, 0.34%]
Overall dihedral [deg]	0	-0.62	Section 3 (twist, max camber)	[0, 0%]	[1.44, 0.53%]
Delta taper break	0.2	0.138	Section 4 (twist, max camber)	[0, 0%]	[-2.23, 0.56%]
Delta c/4 sweep break [deg]	-10	-11.60	Section 5 (twist, max camber)	[0, 0%]	[-0.76, 0.42%]
Wing break location	0.45	0.347			





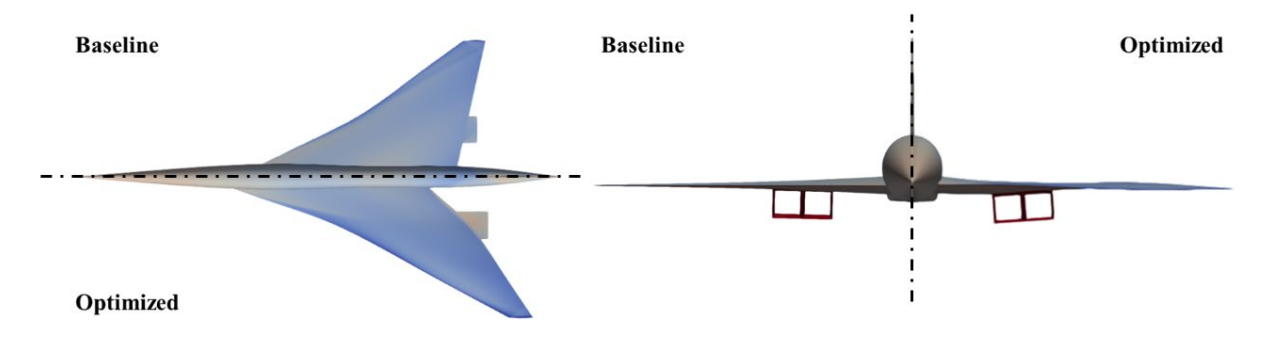


Figure 7. Comparison of baseline and optimized wing planforms.

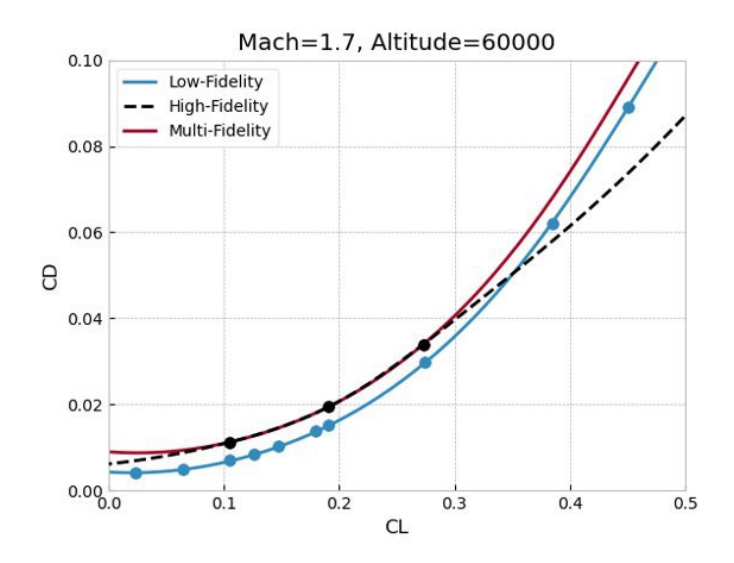


Figure 8. Multi-fidelity drag polar at cruise conditions. CL, lift coefficient; CD, drag coefficient.

Figure 8 shows the multi-fidelity drag polar at cruise conditions for the optimized vehicle. Black points represent the three RANS samples at this flight condition. The high-fidelity curve in this figure shows the drag polar that would have resulted if only the RANS data points were used to fit the surrogate and to extrapolate to the entire flight envelope. Likewise, the blue points are the inviscid data from Cart3D, and the blue low-fidelity curve represents the drag polar obtained from the low-fidelity data only. The red multi-fidelity curve thus depicts the final drag polar for this vehicle, generated by the multi-fidelity surrogate using both inviscid and RANS data. The effect of the multi-fidelity surrogate can be summarized by an upward shift of the inviscid drag polar, which can be attributed to the effect of friction drag.

Eight-pax, Mach-1.4 SST design

The fuselage and VT used for this aircraft remained fixed during the design process. The present aircraft shared the same fuselage as the NASA STCA. The vehicle wing was optimized for this cruise Mach number. The wing design is described below.

The design of the 8-pax vehicle closely follows the approach described previously for the 65-pax vehicle. For this study, the planform area of the wing is fixed at 1,638 ft². In total, 18 geometric variables (Table 3) are considered, and angle of attack is the 19th design variable. The same variables listed in Table 3, are used, with initial generation of 100 warm-start cases. One hundred additional cases are adaptively generated until the expected improvement is below a given threshold. Figure 9 shows the distribution of L/D over the warm-start and adaptive samples. Some adaptive samples with lower L/D (between 5 and 9) correspond to early points in the adaptive sampling, i.e., during the "exploration phase" of the optimization.







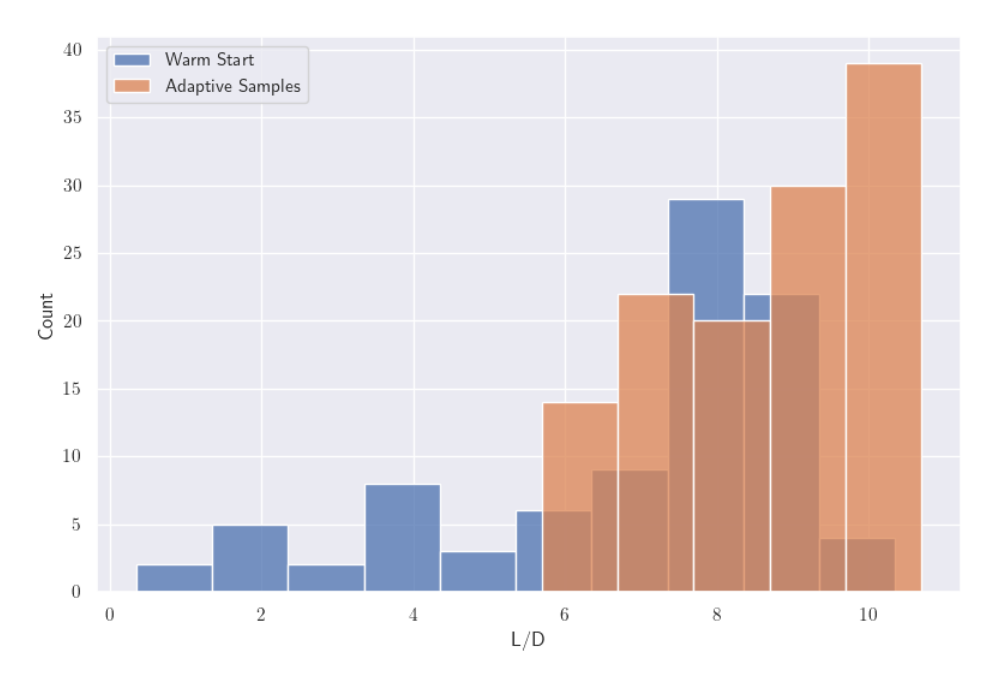


Figure 9. Distribution of lift to drag (L/D) over warm-start and adaptive sampling.

Table 3 below lists the optimized design parameters of the 8-pax, Mach-1.4 SST aircraft, and Figure 10 shows the optimized vehicle geometry.

Table 3. Comparison of baseline and optimized wing design variables (8-pax, Mach-1.4 SST).

Parameter	Baseline	Optimized	Parameter	Baseline	Optimized
Overall taper	0.1	0.114	Delta dihedral break (degrees)	0	1.038
Overall Aspect Ratio (AR)	2.5	2.816	Section 1 (twist, maximum camber)	[0, 0%]	[0.09, 0.99%]
Overall c/4 sweep (degrees)	52.5	55.74	Section 2 (twist, maximum camber)	[0, 0%]	[-1.08, 0.36%]
Overall dihedral (degrees)	0	-0.56	Section 3 (twist, maximum camber)	[0, 0%]	[-0.03, 0.27%]
Delta taper break	0.2	0.28	Section 4 (twist, maximum camber)	[0, 0%]	[-2.44, 0.88%]
Delta c/4 sweep break (degrees)	-10	-5.36	Section 5 (twist, maximum camber)	[0, 0%]	[-1.21, 0.37%]
Wing break location	0.45	0.20			





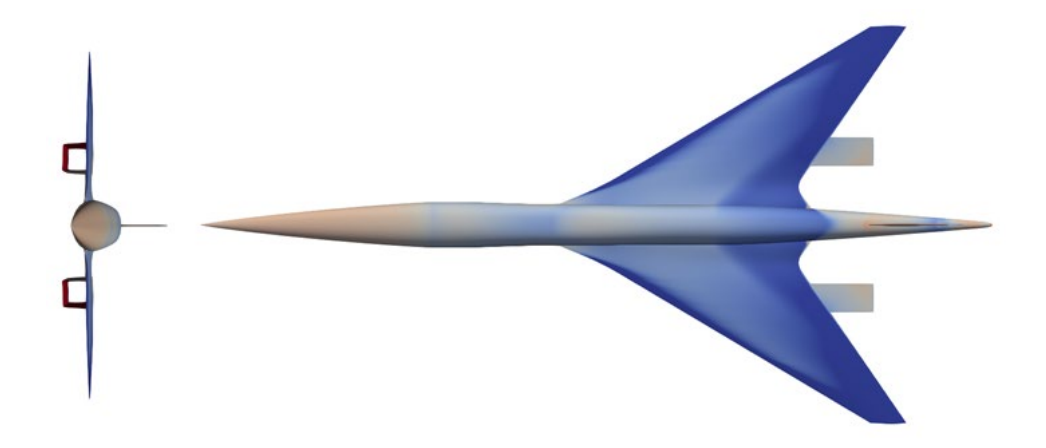


Figure 10. Optimized wing planform for an 8 pax, Mach-1.4 SST.

References

Constantine, P. G., Dow, E., & Wang, Q. (2014). Active subspace methods in theory and practice: applications to kriging surfaces. SIAM Journal on Scientific Computing, 36(4), A1500-A1524.

Forrester, A. I. J., & Keane, A. J. (2009). Recent advances in surrogate-based optimization. *Progress in Aerospace Sciences*, 45(1-3), 50-79. https://doi.org/10.1016/j.paerosci.2008.11.001

Gautier, R., Pandita, P., Ghosh, S., & Mavris, D. (2021). A fully Bayesian gradient-free supervised dimension reduction method using Gaussian processes. *International Journal for Uncertainty Quantification*, 12(2),1-32.

Haimes, R., & Dannenhoffer, J. (2013). The engineering sketch pad: A solid-modeling, feature-based, web-enabled system for building parametric geometry. In 21st AIAA Computational Fluid Dynamics Conference (p. 3073).

Han, Z.-H., & Görtz, S. (2012). Hierarchical Kriging model for variable-fidelity surrogate modeling. *AIAA Journal*, *50*, 1885–1896. <a href="https://doi.org/10.2514/1.]051354

Jones, D. R., Schonlau, M., & Welch, W. J. (1998). Efficient global optimization of expensive black-box functions. *Journal of Global Optimization*, 13(4), 455-492. https://doi.org/10.1023/A:1008306431147

Lee, K., Nam, T., Perullo, C., & Mavris, D. N. (2011). Reduced-order modeling of a high-fidelity propulsion system simulation. AIAA Journal, 49(8). https://doi.org/10.2514/1.j050887

NASA Advanced Supercomputing Division (n.d.) Cart3D Documentation https://www.nas.nasa.gov/publications/software/docs/cart3d/

Seshadri, P., Yuchi, S., & Parks, G. T. (2019). Dimension reduction via gaussian ridge functions. SIAM/ASA Journal on Uncertainty Quantification, 7(4), 1301-1322.

Siemens (n.d.) Simcenter STAR-CCM+. https://www.plm.automation.siemens.com/global/en/products/simcenter/STAR-CCM.html

Tripathy, R., Bilionis, I., & Gonzalez, M. (2016). Gaussian processes with built-in dimensionality reduction: Applications to high-dimensional uncertainty propagation. *Journal of Computational Physics*, 321, 191-223.

Wells, D. P., Horvath, B. L., & McCullers, L. A. (2017). The flight optimization system weights estimation method. NASA/TM-2017-219627

Task 2 - SST Propulsion System Modeling

Georgia Institute of Technology

Objectives

The propulsion system plays a crucial role in predicting performance metrics, including fuel burn, gross weight, and takeoff field length, as well as environmental metrics such as noise and emissions. As such, the objective of this task was to develop a propulsion system model with the following capabilities:

- Predict thrust, fuel flow, and emissions indices as a function of Mach number, altitude, and throttle setting.
- Predict engine dimensions and provide those dimensions to the aerodynamic analysis to assess aircraft drag.
- Predict engine weight and provide that to the overall aircraft empty weight analysis.







Provide the necessary information to the noise analysis model to predict the noise produced by the engine.

Research Approach

The propulsion system developed models a mixed-flow turbofan engine cycle. The engine cycle performance was modeled with NPSS (SwRI, 2025), and the dimensions, flow path, and weight were modeled with Weight Analysis of Turbine Engines (WATE++) (Tong & Naylor, 2008). The following sections outline the engine modeling, analysis, design, and selection process.

Cycle Architecture Selection

A mixed-flow turbofan (MFTF) engine cycle was selected for this work. While modern subsonic aircraft utilize a high-bypass-ratio separate-flow turbofan (SFTF) to enhance overall propulsive efficiency and reduce engine noise, supersonic aircraft tend to favor lower-bypass-ratio engines. One reason is that overall efficiency comparable to high-bypass engines in subsonic flight can be achieved with a lower bypass ratio in supersonic flight. Another reason is that low-bypass engines are smaller and lighter for the same thrust. Given that supersonic engine weight is more sensitive to increases in size (i.e., design mass flow) due to the longer inlets and nozzles required to decelerate and accelerate the flow efficiently, compared to subsonic engines, using a lower-bypass ratio engine helps reduce the higher drag during transonic acceleration and supersonic cruise. To improve performance further, a MFTF modifies a SFTF by mixing the bypass and core flow before exiting through a single exhaust nozzle. Mixing the two streams offers some efficiency gains and higher specific thrust, enabling the engine to not lose thrust as quickly with altitude (Hartmann, 1968; Pearson, 1962). MFTFs have been shown to offer a good compromise of thrust specific fuel consumption (TSFC), jet velocities (i.e., specific thrust), weight, complexity, and fuel burn relative to other cycles such as the turbojet, turbine-bypass engine, and variable cycle engines (Berton et al., 2005; Seidel et al, 1991; Welge et al., 2010). Additionally, this engine type has been proven in both military and civil applications and is the choice of current industry efforts to develop a new commercial supersonic aircraft.

Cycle modeling

The engine cycle performance was modeled using Numerical Propulsion System Simulation (NPSS). A schematic is included in Figure 11, depicting the components in the engine model and their connectivity. The inlet, fan, high-pressure compressor (HPC), turbines, and nozzle were modeled with parametric performance maps. The ATS2 inlet map was selected from the PIPSI/INSTAL library because it covers Mach numbers up to 2.0. The nozzle map selected was the plug nozzle map from the PIPSI/INSTAL library (Kowalski, 1979a). The design efficiencies of the fan and high-pressure compressor are determined through a simple first-stage meanline analysis and a correlation with corrected tip relative Mach number, specific flow, hubto-tip ratio, inlet guide vane angle (if applicable), and pressure ratio. The off-design performance of the fan and high-pressure compressor (HPC) is determined from maps generated using the NASA tool CMPGEN (NASA, n.d.) within the FASST environment thereby eliminating the need for map scaling. The turbine design point efficiencies are also determined through a simple meanline analysis and a correlation with work coefficient, flow coefficient, and degree of reaction based on a notional Smith chart. The turbine off-design performance is determined from scaled notional maps because the FASST environment does not currently include a routine to generate turbine maps parametrically. In addition to performance, the mean line calculation also estimates gross dimensions, number of stages, and RPM, which are required inputs to the engine flowpath and weight analysis.





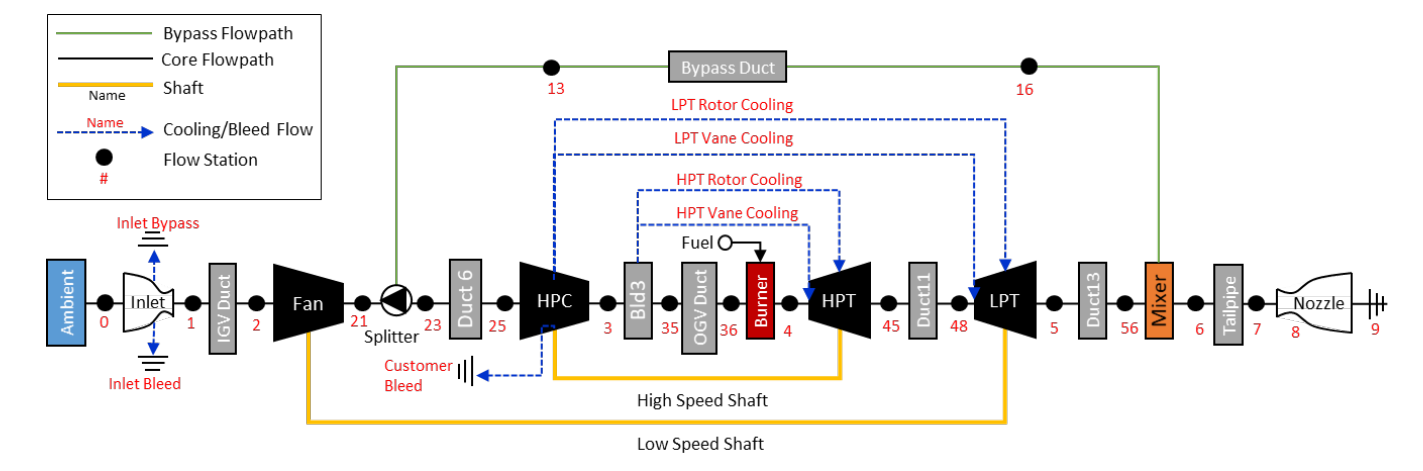


Figure 11. Engine Schematic.

Turbine cooling flows are determined from the NASA-developed Coollt model (Gauntner, 1980), which computes the required cooling flow as a function of metal temperature and the cooling effectiveness parameter $\phi = (T_{gas} - T_{metal})/(T_{gas} - T_{cool})$. Full coverage film cooling is assumed. The rotor blades were assumed to be made of CMSX-4 single-crystal nickel superalloy $(T_{metal} = 2100^{\circ}R)$ and the vanes were assumed to be made of a ceramic matrix composite material $(T_{metal} = 2400^{\circ}R)$. To ensure that the allowable metal temperature used in the cooling flow model was appropriate to the blade stresses experienced, a turbine creep life model was implemented that uses a Larson-Miller correlation to estimate the creep life of the blades, given the metal temperature and predicted stress on the blades (Scholz et al., 2009). The Coollt model also calculates a penalty to turbine efficiency due to cooling.

The loss metrics of the ducts and burner, as well as customer bleed and horsepower extraction, are summarized in Table 4. Duct pressure losses at the design point are assumed, and off-design duct pressure losses are scaled with the square of corrected airflow, as described by Walsh and Flectcher (Walsh & Fletcher, 2004). The mixer loss model is based on the works of Frost (Frost, 1966) and Zola (Zola, 2000) and accounts for momentum losses due to unequal total pressures on the bypass and core sides, friction losses in the mixer chute, and incomplete mixing losses.

Component	Value	Component	Value
Duct 6 Pressure Loss	2.5%	Fuel LHV, [BTU/lbm]	18,580
Duct 11 Pressure Loss	2.0%	Burner Efficiency	99.7%
Duct 13 Pressure Loss	3.0%	Burner Pressure Loss	5.0%
Tailpipe Pressure Loss	2.0%	Customer Bleed, [lbm/s]	0.65 [65pax], 1.95[8pax]
Bypass Duct Pressure Loss	4.0%	Horespower Extraction [hp]	100 [65pax], 112.5[8pax]

Table 4: Cycle Modelling Assumptions.

Cycle Design Methodology

A clean-sheet engine design was conducted as opposed to a fixed-core re-fan design. A clean-sheet engine design means the entire engine is a brand-new design with all of its components sized as required. On the other hand, a fixed-core refan design selects a fixed-core from an existing engine and designs a new low-pressure spool (fan and LPT), inlet, and exhaust system. A simultaneous, multi-design point (MDP) approach was employed in this work to size the engine. Classical single-point analysis sizes the engine at a single flight condition and subsequently iterates to ensure requirements are met at other flight conditions. The MDP method enables simultaneously meeting design requirements and sizing components at multiple flight conditions (Schutte, 2009). The flight conditions considered in this work are listed in Table 5. The Aerodynamic Design Point (ADP) is the sizing point of the engine and a reference point for defining the turbomachinery component performance. The ADP selected in this study is the transonic acceleration point at which having enough thrust is critical to overcome the high drag. The top-of-climb (ToC) point is typically a critical point at which adequate thrust for a minimum specific excess







power is needed. Additionally, this point is part of the supersonic cruise segment, and thus, efficiency is of critical concern. The takeoff point ensures enough thrust at aircraft rotation. The takeoff point is critical to ensure there is enough thrust at rotation with one engine inoperative (OEI). The cooling flow sizing point sizes the turbine cooling flows to the maximum gas and cooling flow temperatures.

Table 5. Thermodynamic Cycle Design Points.

Design Point	Mach	Altitude [ft]	Δ <i>ISA</i> [° <i>F</i>]	Purpose
Aerodynamic Design Point (ADP)	1.2	39,000	0	Size turbomachinery and engine
Top of Climb (ToC)	Design Mach	55,000	0	Match thrust requirements for Top of Climb/Cruise
Takeoff	0.3	0	18	Match thrust requirements for takeoff
Cooling-Flow Sizing	Design Mach	45,000	0	Size cooling flows

The NPSS solver is then used to determine a set of independent parameters (fuel flow, airflow, BPR, etc.) that meet specified target values of specific dependent parameters. A mixed-flow turbofan engine cycle is defined by the following five parameters: fan pressure ratio ($FPR = P_{t21}/P_{t2}$), overall pressure ratio ($PR = P_{t3}/P_{t2}$), top of climb corrected fan speed, max turbine rotor inlet temperature (T_{t41max}), and extraction ratio ($EXTR = P_{t16}/P_{t56}$) (Denney et al., 2005). The ToC corrected fan speed is equivalent to selecting a throttle ratio or ADP turbine rotor inlet temperature. The bypass ratio is another key metric, which is determined by the selection of the above five cycle variables. The ADP airflow is set to meet a TOC thrust requirement subject to constraints on thrust requirements at other points. The thrust requirements are scaled as the vehicle is run through mission analysis. The inlet capture area is sized to ensure the inlet and engine are perfectly matched at TOC. The ranges explored for each of the thermodynamic cycle design variables are included below in Table 6.

Table 6: Thermodynamic Cycle Design Variable Ranges.

Variable	GT 6	5pax	GT 8pax		
	Min	Max	Min	Max	
FPR	1.9	2.5	1.9	2.3	
OPR	20	30	22	35	
Top of Climb Fan %Nc	92%	100%	97%	100%	
T41max	3000	3600	3000	3600	
Top of Climb EXTR	0.9	1.2	0.9	1.15	

Off-Design Power Management

This section describes how the engine was operated for off-design mode through the entire flight envelope. Full power at any flight condition was defined as running the fuel control to target 100% corrected fan speed, constrained by maximum temperature limits on the compressor discharge ($T_{t3max} = 1790\,^{\circ}R$) and turbine rotor entrance. Additionally, the nozzle throat is adjustable and set to maintain the design stall margin. At part power, the fuel flow and fan speed are reduced to hit the thrust target, and the nozzle throat is varied to maintain the design stall margin on the fan. For noise analysis only, the nozzle throat initially reduces thrust at 100% fan speed. This approach is less efficient, but it yields a greater reduction in pressure ratio and jet velocity for the same decrease in thrust. The use of the nozzle throat to maintain 100% fan speed while thrust is reduced is constrained by a choke limit and the maximum throat area, at which point the fan speed is reduced when thrust is decreased. Below a certain power level, a lower fan speed is preferred over a lower fan pressure ratio to reduce fan noise, which is more pronounced during the lower thrust used during approach. The fan operating point is always constrained by limits on the mechanical actuation of the nozzle throat and stall margin limits.





Flowpath and Weight Model

The flowpath and weight of the engine are estimated using a model developed with WATE++. The engine cycle model is run through the entire flight envelope to collect temperature, pressure, mass flow, Mach number, and RPM data that factor into the flowpath and weight analysis. The model predicts the bare engine weight and the weight of a 2D supersonic inlet, nacelle, and an axisymmetric plug nozzle. The inlet weight was modeled using the regressions from PIPSI (Kowalski, 1979b). The nozzle model was modified for an axisymmetric plug nozzle by extending the internal plug outside the nozzle with a 15-degree half-angle and setting the external convergent flap to match the plug half-angle. A custom module for calculating the weights of variable geometry actuators has also been developed. The results of the meanline analysis described earlier are used to estimate the number of stages of turbomachinery required, along with parameters such as hub-tip ratio, area, radii, and blade speeds. As mentioned earlier, the stress predicted by the flowpath model is used to determine the turbine rotor blade creep life and set an appropriate allowable metal temperature.

Results

Table 7 and Table 8 show the propulsion-specific performance characteristics, geometry, and weight for the GT 65pax. Table 9 and Table 10 show the propulsion-specific performance characteristics, geometry, and weight for the GT 8pax. Further details on the vehicle design and selection can be found in Task 5. The results presented below are engine-specific.

Table 7. Engine performance for GT 65pax.

Engine metric	Aerodynamic design point Mach 1.2/39 kft/ISA	Top-of-climb Mach 1.7/55 kft/ISA	Takeoff Mach 0.3/SL/ISA + 18F	Sea-level static uninstalled Mach 0.0/SL/ISA
Fan pressure ratio	2.02	1.94	2.02	2.02
Bypass ratio	3.12	3.22	3.11	3.12
Overall pressure ratio	26.7	24.9	26.6	26.7
Compressor exit temperature (T3; R)	1,377	1,628	1,482	1,413
Burner exit temperature (T4; R)	3,072	3,605	3,252	3,091
Turbine inlet temperature (T41; R)	2,936	3,451	3,111	2,957
Corrected airflow at the fan face (lbm/s)	941.6	911.0	952.6	953.1
Percentage of design corrected fan speed	100.0	98.2	100.0	100.0
Thrust (lbf)	9,565	7,688	30,348	38,995
Thrust-specific fuel consumption $\binom{lbm}{lbf \cdot h}$	0.869	1.023	0.639	0.468
Nozzle pressure ratio	4.27	7.91	1.86	1.82
Jet velocity (ft/s)	1,923	2,429	1,380	1,322

Table 8. Engine geometry and weight for GT 65pax.

Engine geometry variable	Value
Fan diameter (in)	70.2
Inlet capture area (in²)	3,692
Engine pod length (in)	418.5
Engine pod weight (lb)	12,010
Turbomachinery Stages	1-7-1-2





Table 9. Engine performance for GT 8pax.

Engine metric	Aerodynamic design point Mach 1.2/39 kft/ISA	Top-of-climb Mach 1.4/55 kft/ISA	Takeoff Mach 0.3/SL/ISA + 18F	Sea-level static uninstalled Mach 0.0/SL/ISA
Fan pressure ratio	2.02	2.02	2.02	2.02
Bypass ratio	3.67	3.63	3.68	3.70
Overall pressure ratio	27.1	26.9	27.2	27.3
Compressor exit temperature (T3; R)	1,380	1,496	1,484	1,416
Burner exit temperature (T4; R)	3,037	3,395	3,180	2,996
Turbine inlet temperature (T41; R)	2,954	3,330	3,097	2,919
Corrected airflow at the fan face (lbm/s)	668.5	655.2	676.4	676.7
Percentage of design corrected fan speed	100.0	100.0	100.0	100.0
Thrust (lbf)	6,688	3,976	21,101	27,292
Thrust-specific fuel consumption $\binom{lbm}{lbf \cdot h}$	0.836	0.934	0.613	0.441
Nozzle pressure ratio	4.26	5.55	1.86	1.83
Jet velocity (ft/s)	1,900	2,145	1,362	1,304

Table 10. Engine geometry and weight for GT 8pax.

Engine geometry variable	Value
Fan diameter (in)	60.7
Inlet capture area (in²)	2,365
Engine pod length (in)	326.4
Engine pod weight (lb)	8,701.4
Turbomachinery Stages	1-9-1-3

References

Berton, J. J., Haller, W. J., Senick, P. F., Jones, S. M., & Seidel, J. A. (2005). A comparative propulsion system analysis for the high-speed civil. *Nasa/Tm*—2005-213414, *December*.

Denney, R. K., Tai, J. C., Kestner, B. K., & Mavris, D. N. (2005). Variable cycle optimization for supersonic commercial applications. *SAE transactions*, 1354-1361.

Frost, T. H. (1966). Practical bypass mixing systems for fan jet aero engines. Aeronautical quarterly, 17(2), 141-160. Gauntner, J. W. (1980). Algorithm for calculating turbine cooling flow and the resulting decrease in turbine efficiency (No. NASA-TM-81453).

Hartmann, A. (1968). Theory and test of flow mixing for turbofan engines. Journal of Aircraft, 5(6), 522-527.

Kowalski, E. J. (1979a). Computer code for estimating installed performance of aircraft gas turbine engines. Volume 3: Library of maps (No. D180-25481-3-VOL-3).

Kowalski, E. J. (1979b). Computer code for estimating installed performance of aircraft gas turbine engines. Volume 1 (No. D180-25481-1-VOL-1).

SwRI. (2025). Numerical Propulsion System Simulation (NPSS). https://www.swri.org/markets/electronics-automation/software/aerospace-software/numerical-propulsion-system-simulation-npss

NASA. (n.d.). CMPGEN: A Modeling Tool Used to Compute Off-Design Performance Of Fans, Boosters, And Compressors. NASA Technology Transfer Program. https://software.nasa.gov/software/LEW-19686-1

Pearson, H. (1962). Mixing of Exhaust and By-pass Flow in a By-pass Engine. *The Aeronautical Journal*, 66(620), 528-530. Scholz, A., Wang, Y., Linn, S., Berger, C., & Znajda, R. (2009). Modeling of mechanical properties of alloy CMSX-4. *Materials Science and Engineering: A*, 510, 278-283.

Schutte, J. S. (2009). Simultaneous multi-design point approach to gas turbine on-design cycle analysis for aircraft engines. Georgia Institute of Technology.





Seidel, J., Haller, W., & Berton, J. (1991, September). Comparison of turbine bypass and mixed flow turbofan engines for a high-speed civil transport. In *Aircraft Design and Operations Meeting* (p. 3132).

Tong, M. T., & Naylor, B. A. (2008, January). An object-oriented computer code for aircraft engine weight estimation. In *Turbo Expo: Power for Land, Sea, and Air* (Vol. 43116, pp. 1-7).

Walsh, P. P., & Fletcher, P. (2004). Gas turbine performance. John Wiley & Sons.

Wedge, H. R., Bonet, J., Magee, T., Chen, D., Hollowell, S., Kutzmann, A., ... & Tai, J. (2010). N plus 2 Supersonic Concept Development and Systems Integration (No. NF1676L-11057).

Zola, C. L. (2000). Advanced propulsion system studies in high speed research (No. E-12233).

Task 3 - Mission Analysis

Georgia Institute of Technology

Objectives

The objective of mission analysis was to synthesize the results from aerodynamics, propulsion, and weight analyses, to simulate the aircraft dynamics and performance (e.g., fuel burn) over a specific mission. Because the vehicles under consideration are not based on existing vehicles, an additional objective was to size the gross weight, wing, and engine sizes for the specified design range.

Research Approach

As in previous work, Georgia Tech researchers leveraged the FASST modeling and simulation environment to model the supersonic vehicles for this task. This framework was based on the Environmental Design Space (EDS). EDS and FASST have the same goal of providing a modeling and simulation environment that enables trade-offs and interdependencies among aircraft system-level metrics. The difference between them is that EDS was designed for subsonic aircraft; therefore, modifications were implemented to enable the modeling and simulation of supersonic aircraft. In the case of FASST, the system-level metrics of most significant interest are the vehicle weight, design mission fuel burn, and LTO certification noise. The flow diagram for the FASST environment (Figure 12) shows the inputs, outputs, and interconnections among each discipline's analysis module in the modeling and simulation environment.

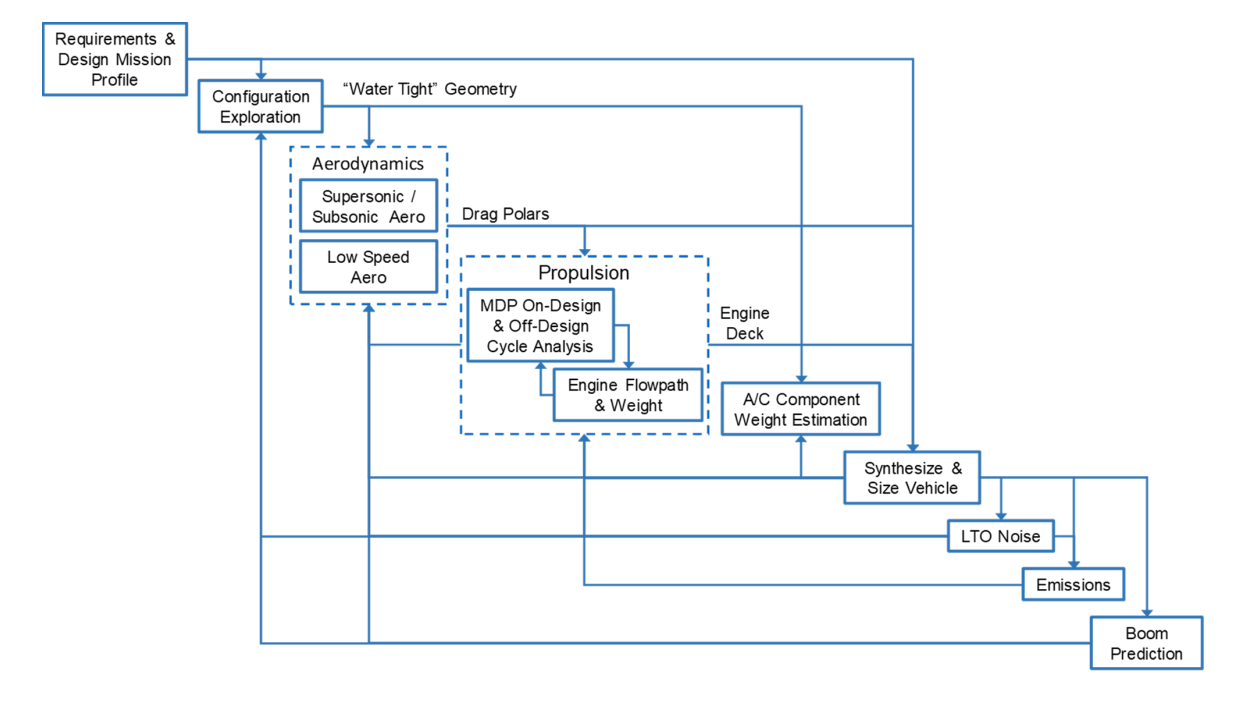


Figure 12. Framework for Advanced Supersonic Transport (FASST) flow diagram.





The requirements and design mission, as specified by the research team, are outlined in the following sections. The high-level requirements for the Mach-1.7, 65-pax SST include the number of passengers (65), the design Mach number (1.7), and the design mission range (4,250 nmi). The high-level requirements for the Mach-1.4, 8-pax SST include the number of passengers (8), the design Mach number (1.4), and the design mission range (4,250 nmi). The configuration exploration and aerodynamics drag polar generation are performed in a local setting outside FASST and are described in Task 1. The resulting drag polars are fed into the mission analysis and vehicle sizing module. The engine cycle modeling is performed in NPSS, and flow path and weight estimation is conducted with WATE++. The engine architecture selected was a mixed-flow turbofan. The propulsion system modeling, discussed in Task 2, provides an engine deck, engine weight, and engine dimensions to the mission analysis and vehicle sizing module. For the vehicle empty weight, mission analysis, and sizing, the NASA code FLOPS is used (McCuller, 1984a). FLOPS uses the inputs of engine deck, drag polar, and other vehicle configuration parameters to estimate the overall empty weight of the aircraft. FLOPS then iterates on the vehicle's gross weight to complete the mission prescribed by the designer. FLOPS also scales the engine thrust and wing area to produce the designer-specified wing loading and thrust loading. If the engine is scaled in FLOPS, it is subsequently rescaled in the engine analysis to obtain an updated engine performance and weight. This iteration continues until the engine no longer requires scaling. After sizing, the vehicle is analyzed through a series of off-design missions.

A paper by NASA provides further descriptions of the mission segments within FLOPS: climb, cruise, refueling, payload releases, accelerations, turns, hold, and descent (McCullers, 1984b). Many of these mission segments were developed for modeling military aircraft. The mission segments used in this study are climb, cruise, loiter, and descent. The performance of each segment is determined using a step integration method to compute fuel burn, elapsed time, distance covered, and changes in speed and altitude. The mission consists of a 9-minute taxi-out time at ground power setting, a 1-minute takeoff at takeoff power, a minimum fuel climb and acceleration to supersonic cruise, a supersonic cruise-climb, a descent at maximum L/D ratio, and a taxi-in time of 5 min at ground power. A reserve mission is also flown, which consists of a missed approach, a 200-nmi reserve mission to an alternative airport, and a 30-minute hold at Mach 0.38 and 6,000 ft. The reserve mission to an alternative airport consists of a minimum fuel climb to an optimal subsonic cruise altitude below 30,000 ft and Mach 0.95, a cruise at optimum Mach and altitude, and a descent at maximum L/D. The reserve fuel has an additional safety margin of 5% of total trip fuel. The mission is constrained by a maximum altitude of 60,000 ft, a maximum Mach number equal to the design Mach number, and a maximum dynamic pressure limit of 600 psf. Additionally, the aircraft is not allowed to fly faster than 250 KCAS when below 10,000 ft. Although not part of the synthesis and sizing process, the detailed LTO module of FLOPS is used to provide detailed information on the LTO trajectories for both 14 CFR Part 25 performance and 14 CFR Part 36 LTO noise analysis. The LTO noise prediction is discussed in the next task (Task 4, LTO Noise Modeling).

Results

The block mission profile for the Mach-1.7 SST carrying 65 pax for 4,250 nmi (excluding the reserve mission) is depicted in Figure 13. The aircraft begins by accelerating and climbing to 250 KCAS and 10,000 ft, in accordance with Federal Regulation (14 C.F.R. § 91). The aircraft then accelerates at nearly constant altitude until it encounters the dynamic pressure limit. The aircraft then primarily climbs and accelerates at constant dynamic pressure, deviating from the dynamic pressure limit for only short periods of time. After reaching Mach 1.7, the aircraft continues the climb at a constant Mach number until it reaches the optimal cruise altitude or the altitude at which it has 300 fpm of excess power. The aircraft performs a cruise-climb from 49,907 ft to 56,929 ft. The aircraft then descends at maximum L/D. In doing so, the aircraft initially decelerates at constant altitude until approximately Mach 1.3, then both descends and decelerates beyond that point. The reserve-mission cruise is conducted at Mach 0.88 and at 30,000 ft. A similar profile is shown for the Mach 1.4 8-pax vehicle in Figure 14. A weight breakdown for each of the vehicles is provided in Table 11 and Table 12.





Table 11. GT-65pax Vehicle Weight Breakdown.

Weight Item	Weight (lb)
Wing	83,360
Vertical tail	2,303
Fuselage	31,115
Landing gear	19,306
Structure total	136,083
Engines	48,048
Thrust reversers	5,014
Miscellaneous systems	1,665
Fuel system	3,050
Propulsion total	57,778
Surface controls	6,858
Auxiliary power	888
Instruments	1,091
Hydraulics	3,202
Electrical	3,804
Avionics	1,852
Furnishings and equipment	15,023
Air conditioning	3,512
Anti-icing	432
Systems and equipment total	36,662
Weight, empty	230,523

Weight Item (continued)	Weight (lb)
Crew and baggage (two flight, two cabin)	760
Unusable fuel	1,251
Engine oil	320
Passenger service	2,245
Cargo containers	604
Operating weight	235,703
Passengers and baggage (65)	13,650
Zero fuel weight	249,353
Taxi-out fuel	1,338
Takeoff fuel	1,102
Climb fuel	25,524
Cruise fuel	125,489
Descent and landing fuel	4,033
Missed-approach fuel	2,203
Reserve-mission fuel	19,001
Hold fuel	10,028
Mission fuel	186,515
Ramp weight	435,868

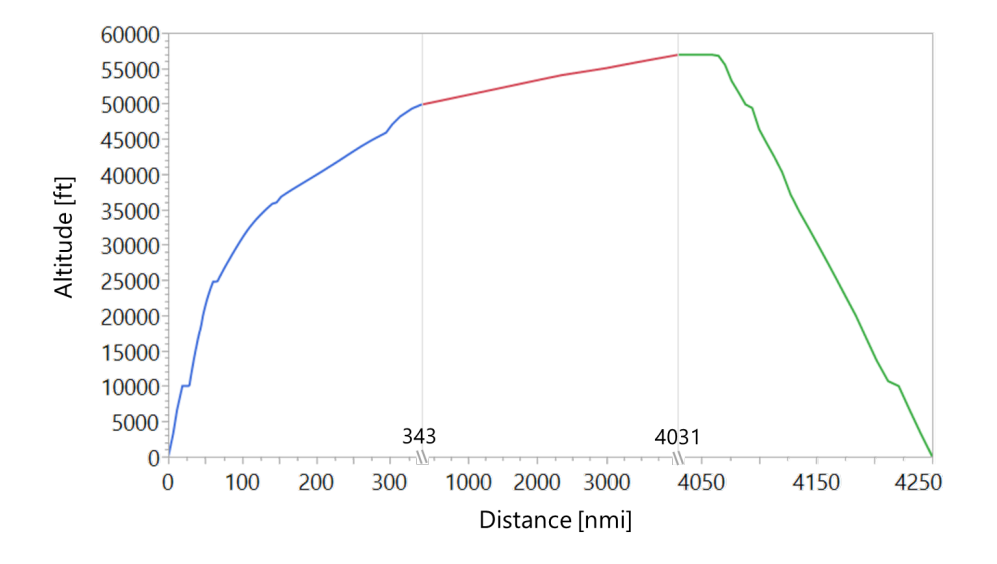


Figure 13. Mission profile for GT-65pax supersonic transport





Table 12. GT-8pax Vehicle Weight Breakdown.

Weight Item	Weight (lb)
Wing	13,453
Vertical tail	534
Fuselage	9,695
Landing gear	3,889
Structure total	27,570
Engines	17,397
Thrust reversers	1,525
Miscellaneous systems	548
Fuel system	866
Propulsion total	20,336
Surface controls	1,808
Auxiliary power	471
Instruments	510
Hydraulics	1,048
Electrical	1,549
Avionics	1,181
Furnishings and equipment	2,340
Air conditioning	1,132
Anti-icing	188
Systems and equipment total	10,227
Weight, empty	58,134

Weight Item (continued)	Weight (lb)
Crew and baggage (two flight, two cabin)	760
Unusable fuel	532
Engine oil	110
Passenger service	251
Cargo containers	175
Operating weight	59,962
Passengers and baggage (65)	1,680
Zero fuel weight	61,642
Taxi-out fuel	443
Takeoff fuel	625
Climb fuel	4,395
Cruise fuel	37,418
Descent and landing fuel	2,048
Missed-approach fuel	735
Reserve-mission fuel	2,643
Hold fuel	2,368
Mission fuel	50,675
Ramp weight	112,317

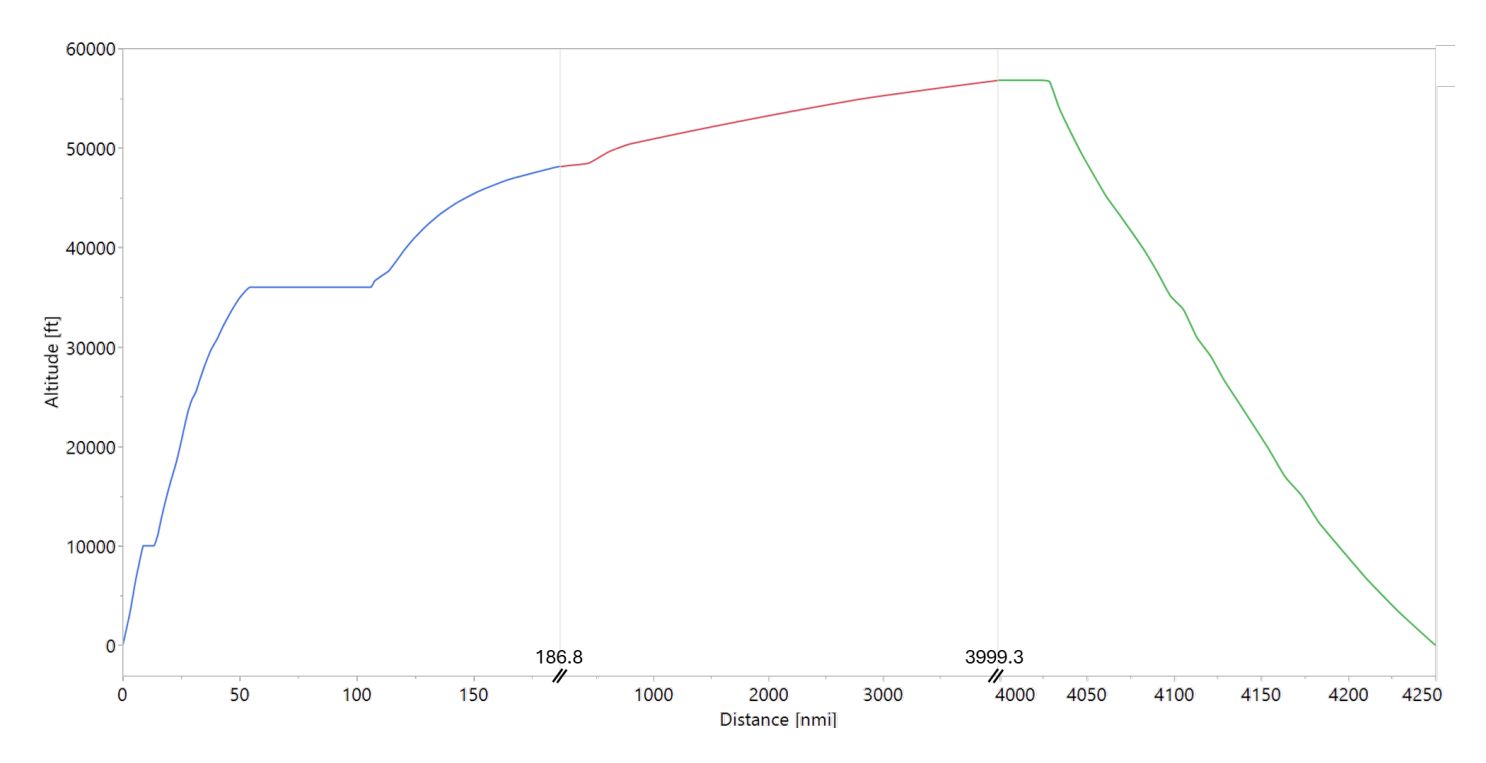


Figure 14: Mission profile for GT-8pax supersonic transport.





References

General Operating and Flight Rules, 14 C.F.R. § 91 (2025). https://www.ecfr.gov/current/title-14/chapter-l/subchapter-F/part-91

McCullers, L. A. (1984a). Aircraft configuration optimization including optimized flight profiles. NASA. Langley Research Center Recent Experiences in Multidisciplinary Analysis and Optimization, Part 1.

McCullers, L. A. (1984b). Aircraft configuration optimization including optimized flight profiles. NASA. Langley Research Center Recent Experiences in Multidisciplinary Analysis and Optimization, Part 1.

Task 4 - LTO Trajectory and Noise Modeling

Georgia Institute of Technology

Objective

The objective of this task was to simulate an aircraft's LTO trajectory by using a VNRS to study the effects of different takeoff procedures on LTO noise.

Research Approach

LTO trajectory analysis is performed in FASST after the mission analysis sized the vehicle for the design mission. The LTO trajectory analysis uses the detailed LTO module from the NASA code FLOPS. The aircraft is flown with a VNRS procedure consisting of a series of pilot-initiated and automatic (i.e., no pilot control) changes to engine and airframe configurations during a takeoff run to help reduce noise.

For the detailed takeoff analysis, FLOPS numerically integrates the equations of motion, reproduced as Equations (2)–(6), on the basis of the assumption that the aircraft is a point mass with a free-body diagram similar to that in Figure 15.

$$\frac{ds}{dt} = V_{\infty} \cos \gamma \tag{2}$$

$$\frac{dh}{dt} = V_{\infty} \sin \gamma \tag{3}$$

$$m\frac{dV_{\infty}}{dt} = T(V_{\infty}, h, \theta)\cos\alpha - D(V_{\infty}, h, \alpha) - W\sin\gamma$$
(4)

$$m\frac{dV_{\infty}^{2}}{dr_{v}} = mV_{\infty}\frac{d\gamma}{dt} = L(V_{\infty}, h, \alpha) + T(V_{\infty}, h, \theta)\sin\alpha - D(V_{\infty}, h, \alpha) - W\cos\gamma$$
(5)

$$\frac{dW}{dt} = -\frac{dW_f}{dt} = -T(V_{\infty}, h, \theta)TSFC(V_{\infty}, h, \theta)$$
(6)

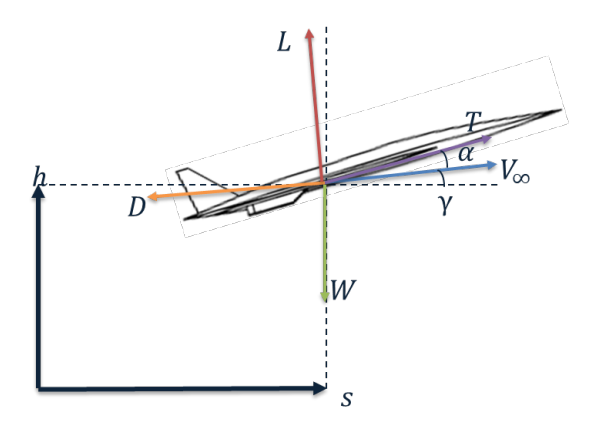


Figure 15. Free-body diagram.





The VNRS takeoff procedure is parameterized by several characteristics, optimized the aircraft's acceleration on the ground and post obstacle and the programed lapse rate post obstacle to minimize the takeoff noise. The first characteristic is the initial power reserve (identified by the FLOPS variable VARTH). Next additional ground acceleration before rotation can be performed (designated as ΔV_R in Figure 16 and Figure 17), although configuration specific, acceleration on the ground may be more efficient than acceleration in the air, (ground acceleration has rolling drag to consider, but in air acceleration has greater lift induced drag to overcome), and additionally higher initial liftoff speed may prove beneficial to initial in air segments. The next element is the programmed high-lift device (PHLD) schedule. The PHLD consists of a flap deflection schedule optimized for the aerodynamic efficiency for the required lift at each point in the takeoff trajectory, which is controlled by the flight management system. The programmed thrust lapse rate (identified by the FLOPS variable PLR) is a thrust reduction that is automatically controlled by Full Authority Digital Engine Control (FADEC). In the framework of VNRS, both the PHLD and the PLR are implemented immediately after the aircraft clears the obstacle during takeoff and must be completed before the measurement period of the noise observers begins. The final few parameters pertain primarily to the trajectory taken after clearing the obstacle; these parameters are the flight-path angle post obstacle (γ_2), the time spent accelerating after PLR is completed (Δt_a) , and ground track distance flown once constant speed segment has begun until cutback is performed (Δd_{cb}). It is important to note, that this parameterization was created to enable the design space exploration discussed in task 5 as defining everything as a delta minimized implausible trajectories considered by the design space exploration. Should this trajectory actually be flown, for example, a pilot would likely not track the time spent accelerating after PLR is completed and instead would likely use speed or altitude targets to decide to transition to a constant speed climb. A schematic of this procedure is depicted in Figure 16 and Figure 17.

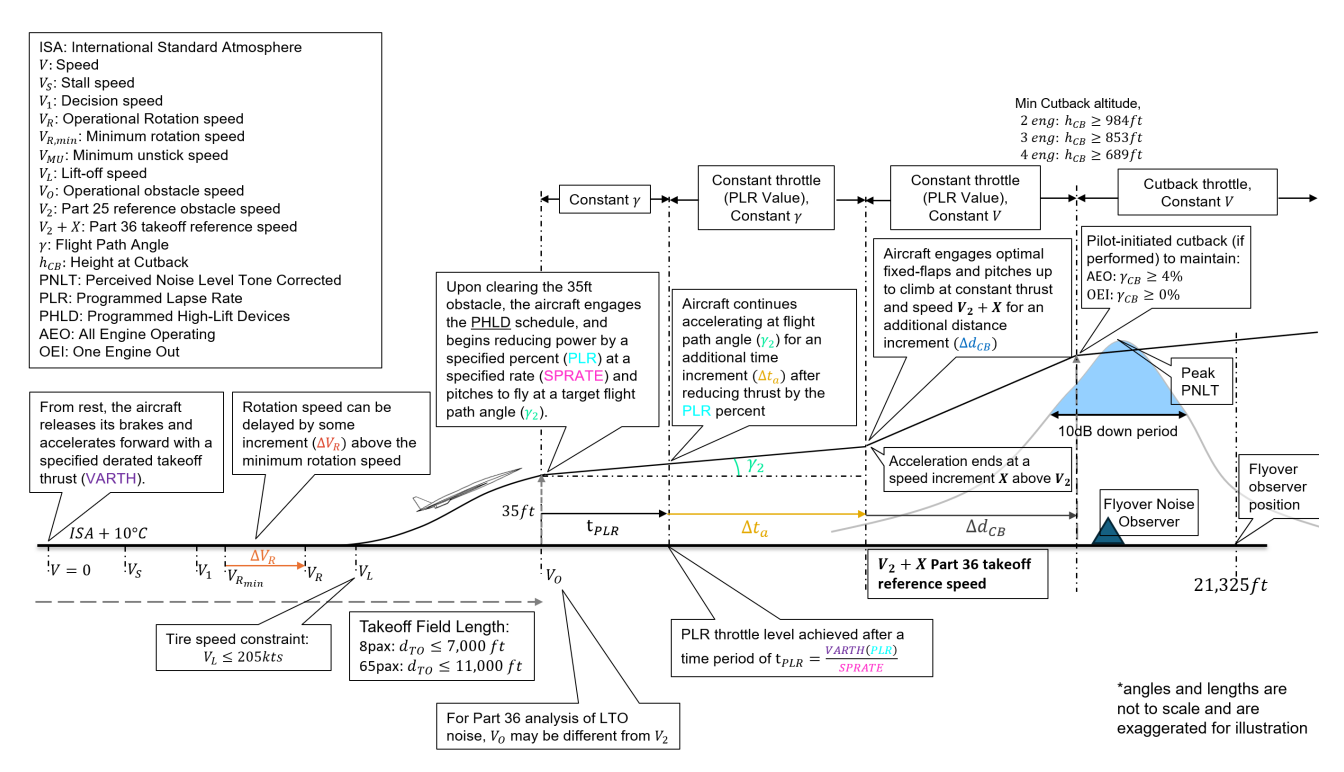


Figure 16. VNRS takeoff procedure with a Cutback (used for flyover noise measurements).



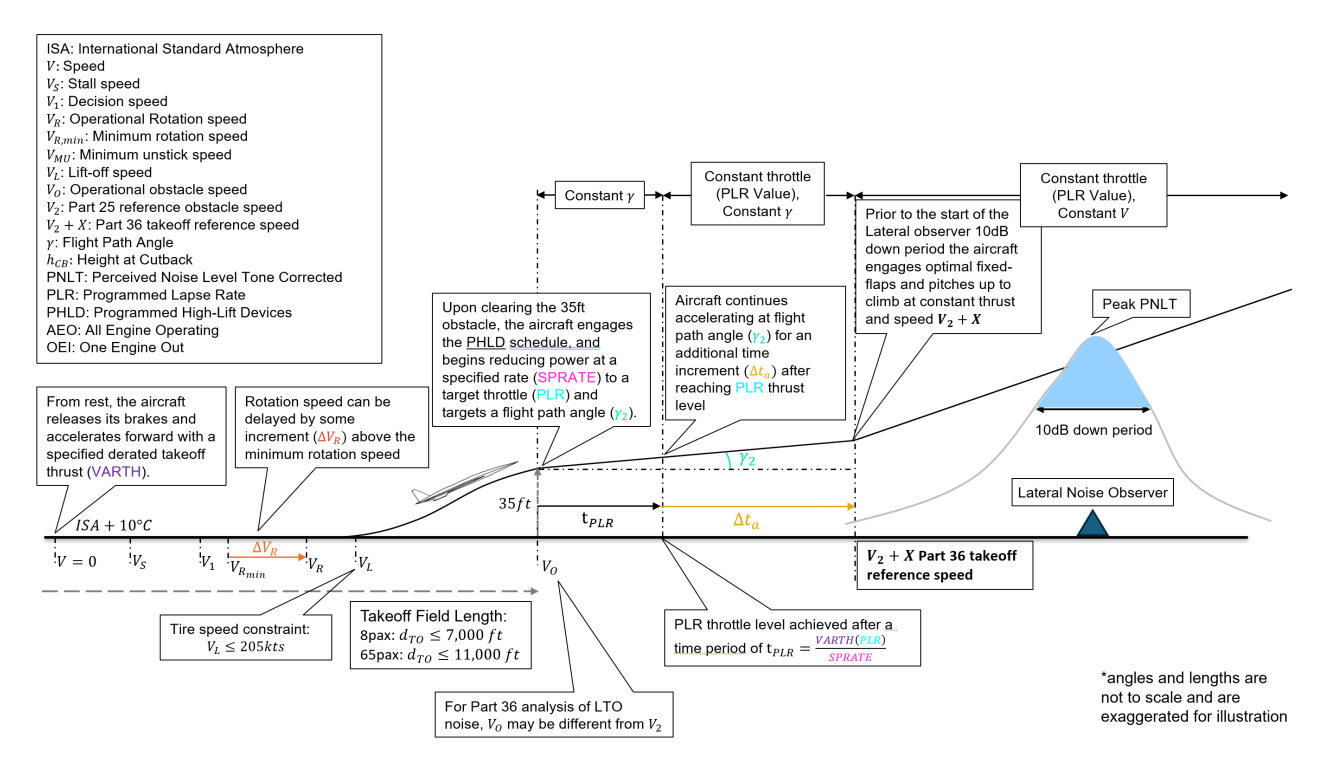


Figure 17. VNRS takeoff procedure without a Cutback (used for lateral noise measurements).

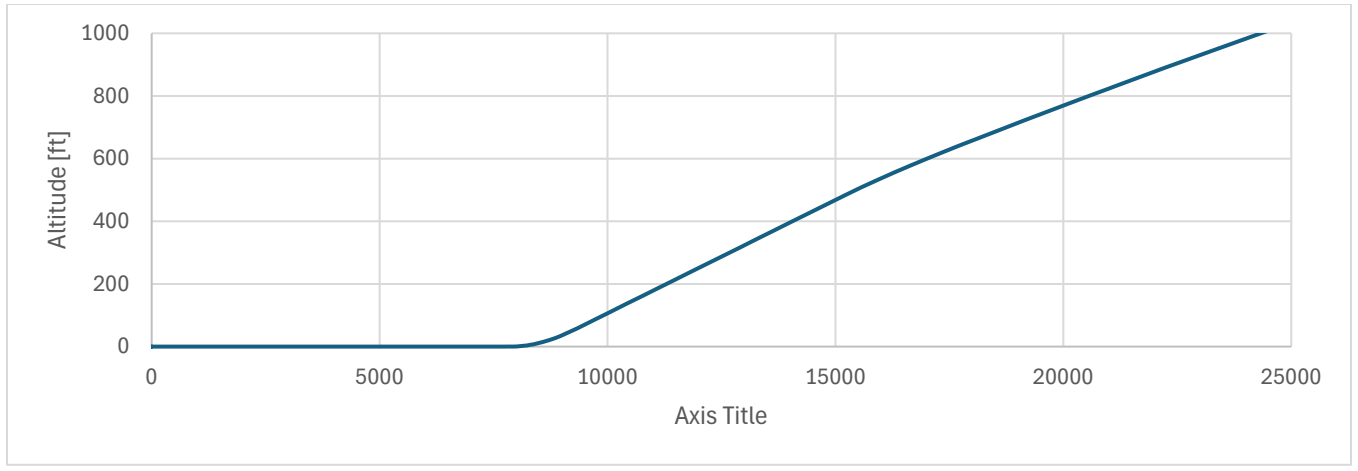
The takeoff trajectory is simulated as follows:

- 1. From a resting position, the aircraft releases its brakes and accelerates forward with a specified power reserve.
- 2. After reaching the unstick velocity, (within a safety margin and including any additional delay from the VNRS procedure), the aircraft starts to increase the angle of attack.
- 3. After the lift force produced exceeds the weight of the aircraft, the aircraft lifts off from the runway. The aircraft then starts flying at a constant speed until it reaches the obstacle altitude of 35 ft.
- 4. After clearing the obstacle, the aircraft engages the PHLD schedule, reduces power to the specified lapse rate, and switches to a constant thrust flight at a prescribed flight-path angle.
- 5. After completing the thrust reduction procedure, the aircraft continues to accelerate until a target speed to achieved, upon which the aircraft transitions into a fixed speed climb.
- 6. Finally, at a second prescribed altitude, the aircraft performs the pilot-initiated cutback and then maintains the current settings until it flies off the aerodrome (50,000 ft distance from break release). The cutback thrust is calculated internally, such that the thrust is sufficient to maintain a 2.29° (i.e., 4% gradient) flight-path angle with all engines operating and to maintain level flight with one engine inoperative. When lateral noise is being certified, the engine thrust reduction is not simulated, but in normal operations this thrust reduction is included.

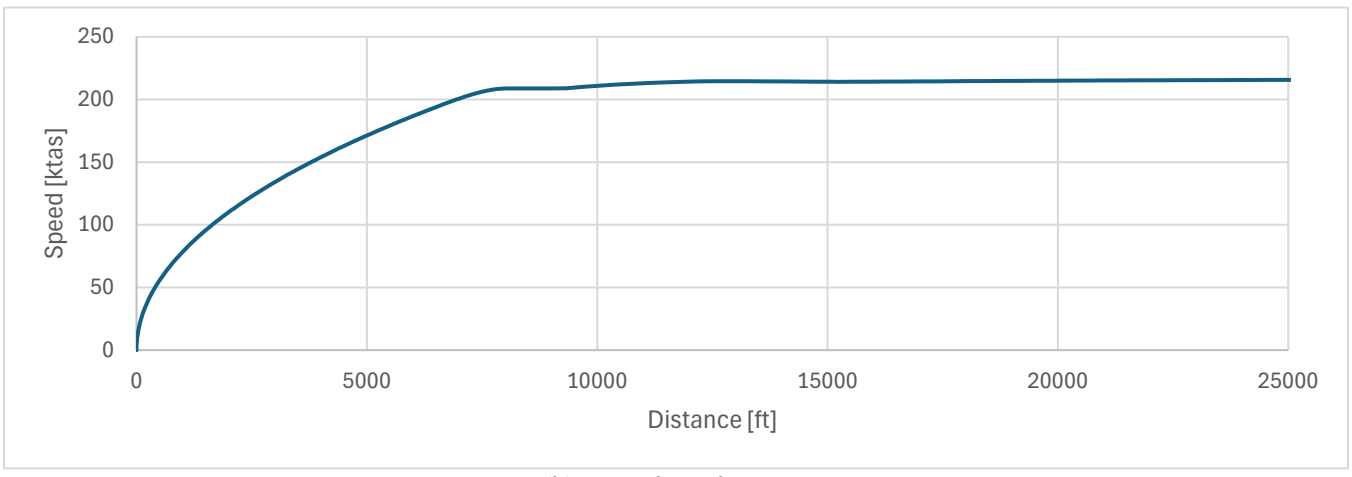
NASA's FLOPS detailed LTO module is used to predict the vehicles LTO trajectory according to the prescribed VNRS procedure parameters. A notional visualization of this simulation is shown in the plots in Figure 18.



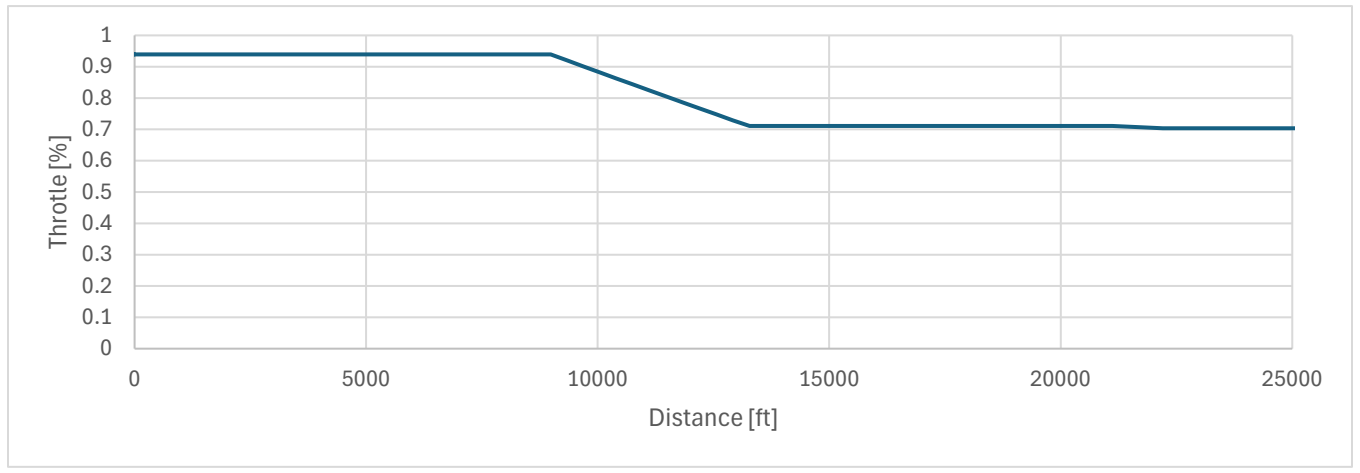




(a) Altitude vs. distance



(b) Speed vs. distance



(c) Throttle vs. distance

Figure 18. Notional VNRS takeoff.







Federal regulation Part 25.107(c) indicates the requirements for V_2 are as follows: " V_2 , in terms of calibrated airspeed, must be selected by the applicant to provide at least the gradient of climb required by § 25.121(b) but may not be less than— (1) V_{2min} ; (2) VR plus the speed increment attained (in accordance with Part 25.111(c)(2)) before reaching a height of 35 feet above the takeoff surface; and (3) A speed that provides the maneuvering capability specified in § 25.143(h)" (14 C.F.R. § 25, 2025). V_{2min} is defined according to stall speed and is calculated internally in FLOPS, whereas V_R plus the speed increment attained before reaching a height at 35 ft is taken as the speed at which the vehicle clears the obstacle. While the VNRS procedure contains the option to delay rotation and gain additional speed on the ground, V_2 , is calculated from a takeoff with no rotation delay in order to make V_2 consistent across all takeoff procedures for an aircraft.

The Georgia Tech team does not examine maneuvering capabilities beyond those internally calculated by FLOPS. $V_2 + X$, the part 25 takeoff reference speed, is calculated as the fixed climb speed in KCAS after post obstacle acceleration is completed, with the X value being defined as the speed above V_2 . Georgia Tech explored how various X values effected takeoff performance, but Georgia Tech enforced an optimization constraint such that the value of X should not be less than 10 KEAS, and $V_2 + X$ must respect the 250-KEAS terminal area speed limit below 10,000 ft MSL, according to federal regulation Part 91.117(a) (14 C.F.R. § 91, 2025). In addition, in accordance with Appendix B to 14 CFR Part 36, specifically section B36.7(b)(1)(ii)(A), a lower-bound constraint is enforced to accept only designs in which the pilot-initiated cutback altitude (identified as h_4 in Figure 17) is greater than 689 ft for aircraft with 2 engines, 853 ft for aircraft with 3 engines, and 984 ft for aircraft with 4 engines (14 C.F.R. § 36, 2025).

During Noise Certification procedures, a component EPNL measurements is a duration correction in which Noise measurements are summed over a period where noise readings are within 10 dBs of the peak perceived noise level tonecorrected value. This procedure is defined in 14 CFR Appendix A to Part 36 section 4.5.1 (14 C.F.R. § 36, 2025). This measurement period, which will hence be referred to as the 10-dB down period and there are multiple requirements for the 10-dB down period in Part 36 and FAA Advisory Circular 36-4D. The requirements are as follows: Maximum Variation on Airspeed as specified by 14 CFR Appendix B to Part 36 section 8 (g); Limits on Crosswind Velocity as defined by 14 CFR Appendix A to Part 36 section 2.2.2 (e); limits on ambient noise as specified by 14 CFR Appendix A to Part 36 section 3.10.2; Requirements for flight path measurements as specified by 14 CFR Appendix A to Part 36 section 3.10.2; and a requirement for stable conditions for a stable configuration as specified by the FAA Advisory Circular 36-4D section AMC A2 4.5 (14 C.F.R. § 36, 2025 and Federal Aviation Administration, 2017). In trajectory simulations Georgia Tech checks to ensure rules regarding 10-dB down period are respected, if they are violated, the trajectory is considered invalid. Crosswind Velocity, Ambient Noise, and Flight Path Measurements are not a concern for simulation environments as these can be turned off or controlled as a part of the simulation. Although 14 CFR Appendix B to Part 36 section 8 (g) allows for a 3% variation in airspeed during the 10 dB down period during flight testing engines (14 C.F.R. § 36, 2025), Georgia Tech is requiring that the airspeed be constant. To compile for the requirement of a stable configuration Georgia Tech ensures that a consistent throttle setting is reached and variable flaps are disengaged before entering the 10-dB down period. FAA Advisory Circular 36-4D ETM 4.2.1.2.1 describes the procedure for a cutback maneuver to reduce flyover noise, so a throttle reduction for this procedure is not taken to not violate the requirement the 10-dB down period for the flyover observer. Additionally, Georgia Tech is assuming that a variable nozzle would be compliant with a stable configuration. Georgia Tech assumes that Flyover and Lateral noise measurements are performed in separate takeoff, so the cutback procedure does not affect the lateral 10dB down period.

Finally, the noise assessment for each aircraft configuration is performed with NASA's program ANOPP. The resulting trajectory and aircraft state along the trajectory (thrust, angle of attack, altitude, distance, speed, etc.) is passed from the FLOPS analysis to ANOPP. In performing these assessments, several assumptions are made in selecting and using different ANOPP modules. Table 13 presents a breakdown of the ANOPP input file structure and the rationale applicable to each module or section.





Table 13. Modules used in aeroacoustics analysis.

Component	ANOPP module	Acronym	Rationale
Trajectory	Source Flyover Module	SFO	Separate trajectories (prescribed by FLOPS) were considered for the sideline and the cutback/approach noises assessments. The difference was that the sideline trajectory did not include a cutback section after the second-segment acceleration; both cases used a VNRS takeoff trajectory.
Airframe	Fink's Airframe Noise Module	FNKAFM	This module was used to predict the broadband noise from the dominant components of the airframe, on the basis of a method developed by Fink for the FAA.
Jet	Single Stream Circular Jet Noise Module	SGLJET	The single-stream jet mixing noise was calculated with a method based on SAE ARP 876, which is known to be the best representation of the current nozzle type.
Fan	Heidmann Fan Noise Module	HDNFAN	The fan inlet and discharge noises were assessed separately for their tone and broadband contributions, with a method based on correlations to model and full-scale test data.
Treatment	Fan Noise Treatment Module	TREAT	Given that the chosen fan module is based on the assumption that the inlet and discharge ducts have no acoustic treatment internal to HDNFAN, the attenuation spectra were applied to separate predictions of the inlet and aft radiated source noise produced by the source noise module, and a total attenuated fan noise prediction was produced.
Combustor	Combustion Noise Module	GECOR	The combustor noise was predicted with a method developed by General Electric and later adopted by the SAE A-21 Committee.
Shielding	Wing Module	WING	This module was used to compute the geometric effects of wing shielding or reflection on the propagation of engine noise (depending on the engine placement/configuration).

Results

The key metric of merit for the LTO analysis for design/cycle selection is certification effective perceived noise level. The results of the analyses provide a procedure, trajectory, aircraft state, and effective perceived noise level for the three noise-certification observers (sideline/takeoff, cutback/flyover, and approach), the noise margin relative to Chapter 14 for each observer, and the cumulative sum. These results are used in Task 5, Engine Cycle and Takeoff Trajectory Space Exploration, to understand how different trajectories affect LTO noise and to quantify a Pareto front between fuel burn and LTO noise.

References

Airworthiness Standards: Transport Category Airplanes, 14 C.F.R. § 25 (2025). https://www.ecfr.gov/current/title-14/chapter-I/subchapter-C/part-25

Federal Aviation Administration. (2017). Noise Standards: Aircraft Type and Airworthiness (36-4D). https://www.faa.gov/regulations_policies/advisory_circulars/index.cfm/go/document.information/documentid/10 31948

General Operating and Flight Rules, 14 C.F.R. § 91 (2025). https://www.ecfr.gov/current/title-14/chapter-I/subchapter-F/part-91

Noise Standards: Aircraft Type and Airworthiness Certification, 14 C.F.R. § 36 (2025). https://www.ecfr.gov/current/title-14/chapter-I/subchapter-C/part-36

Task 5 - System Design Space Exploration and Optimization

Georgia Institute of Technology

Objective

The objective of this task was to explore a design space consisting of engine cycle, vehicle sizing, and LTO operational parameters to explore various questions regarding how changes to these variables affect different response metrics of interest. Previous Annual Reports for Ascent 10 have established an interdependency between fuel burn and LTO noise.







Those studies' goal was to find a Pareto front (i.e., set of non-dominated designs, such that any other potential design is worse in at least one objective) between the objectives of design block fuel burn and cumulative LTO noise margin. However, this year will focus on selecting and optimizing single design point which minimizes fuel at the minimum acceptable noise, (5 EPNdB Margin to Chapter 14 to allow for a buffer for some uncertainty), and then exploring how changes to the takeoff reference speed $V_2 + X$ (typically $V_2 + 10$ kts) affect the certification noise levels. Through engine cycle and takeoff trajectory design space exploration, these questions can be answered to allow policymakers to understand the implications of setting regulatory limits and enable designers to better understand how to design vehicles to meet various potential regulatory thresholds.

Research Approach

All modeling elements described previously make up the modeling and simulation environment called FASST. FASST is used as the analysis tool to predict objectives (e.g., block fuel and LTO noise margin) and constraints (e.g., $V_z + X$, takeoff field length, approach speed, span, etc.) as a function of the design variables. The design space exploration and multi-objective optimization described in the following paragraphs use a design space consisting of engine cycle, vehicle sizing, and LTO operational variables. Airframe design variables were not considered in this task, because the airframe geometry design was optimized separately, as described in Task 1. However, because the aircraft was sized in FLOPS for thrust loading and wing loading over a design mission range of 4,250 nautical miles, the wing size and engine size change. The effects of changes in the size of the wing and engines on aerodynamics was captured by the parametric drag polar described in Section 1. The effects of wing weight changes are handled by the FLOPS weight equations, and changes in engine weight are handled by WATE++ (Tong & Naylor, 2008; Wells et al., 2017). The engine cycle variables consist of the fan pressure ratio, overall pressure ratio, extraction ratio, top-of-climb corrected fan speed, and maximum turbine rotor inlet temperature. The fan pressure ratio and overall pressure ratio are typical parameters for a turbofan. The extraction ratio, the total pressure ratio at the mixer entrance between the bypass and the core, was used to determine the bypass ratio, because keeping the extraction ratio in the vicinity of 1 is generally desirable. The maximum turbine rotor inlet temperature is generally an operational limit but should be set to balance cooling air penalties with the performance benefits of the higher gas temperature. Because the maximum turbine rotor inlet temperature was treated as a design variable rather than a constant, the top-of-climb percentage corrected fan speed, rather than the throttle ratio, was used as the parameter determining the design point turbine rotor inlet temperature. The use of a top-of-climb fan speed target is similar to procedures used during the High-Speed Research (HSR) program, wherein a top-of-climb mass flow lapse was used as a design parameter (Pratt and Whitney and General Electric Aircraft Engines, 2005). Standard vehicle sizing parameters of thrust loading and wing loading are also treated as design variables. The thrust loading was defined as the ratio of the 100%-corrected fan speed thrust at sea-level static to the takeoff gross weight of the aircraft. The wing loading is the ratio of the takeoff gross weight of the aircraft to the wing area. LTO operational parameters consist of the Takeoff Thrust Derate, a Rotation Delay, Programed Lapse Rate, Engine Spool Rate, second-segment flight-path angle, Acceleration Time, and pilot-initiated cutback location. Tasks 2, 3, and 4 provide further details on the definitions of these variables and the analyses. Altogether, 14 parameters were considered (summarized in Table 14).

The first phase involved constructing a Latin-hypercube DoE to generate a large set of design alternatives. Each of the designs was simulated with FASST. To accelerate the simulation time, HTCondor was used to distribute the simulations across ~1,700 cores (HTCondor, n.d.). This allowed for simulations of 10s of thousands of cases within a manageable amount of time. The results were analyzed and plotted in JMP v16 (SAS Institute Inc., n.d.). Design variable ranges were refined, and additional data were generated as necessary. These data points were used to generate neural-network surrogate models, by using JMP, to represent both objectives and constraints which are summarized in Table 15. The objective considered was the block fuel of the design mission, which is the fuel from the beginning of taxi-out at departure to the end of taxi-in at destination but does not include the reserve mission. The mission analysis section provides more details on calculation of the design block fuel. The cumulative noise is the sum of the three LTO observers (takeoff/sideline, flyover/cutback, and approach). The cumulative LTO noise margin is the difference between the allowable cumulative LTO noise for stage 5/chapter 14 and the actual cumulative LTO noise. More details on how the noise was calculated are provided in Task 4. The takeoff field length is the FAR takeoff field length or balanced field length; this is the distance from brake release to reaching 35 ft altitude if an engine is lost at the decision speed V_1 and is also equal to the distance to stop if the takeoff is aborted after engine failure at V_1 . The landing field length is the FAR landing field length, which is determined by dividing the calculated landing field length by 0.6 to account for variations in landing conditions. The approach speed is the aircraft's airspeed for a 3° glide slope in the landing configuration and at landing weight. The approach speed is constrained for a category D aircraft according to the United States Standard for Terminal Instrument Procedures. The aircraft wingspan is constrained to fit in category III gates, as defined in FAA Advisory Circular 150/5300-13. The second-segment thrust is the excess thrust available for a 3% climb gradient with gear up at V_2 ; this is constrained to be greater than zero to ensure sufficient thrust. The speed





below 10,000 ft is constrained to less than 250 KCAS. The distance at which cutback occurs is constrained to occur before the position of the cutback observer. The post-obstacle acceleration is constrained to ensure that the aircraft climbs at a speed of at least $V_2 + 10$ kts. In previous years, LTO noise was treated as the second objective, with the 2021 demonstrating the pareto front that can exist between block fuel and noise margin, but the decision was made for the study this year to consider noise as a constraint and select the design with the lowest block fuel that had at least a 5 EPNdB Noise margin and satisfied all other constraints.

Table 14. Design variables.

Engine cycle variables	Vehicle sizing variables	LTO operational variables	
1. Fan pressure ratio	6. Thrust loading	8. Takeoff thrust derate	
2. Overall pressure ratio	7. Wing loading	9. Delayed Rotation	
3. Extraction ratio (i.e., bypass ratio)		10. Programmed Lapse Rate (PLR)	
4. Maximum turbine inlet temperature		11. Engine Spool Rate	
5. Top-of-climb corrected fan speed (i.e., throttle		12. Initial Flight Path Angle	
ratio or design turbine inlet temperature)		13. Acceleration Time	
		14. Cutback Location	

Table 15. Objectives and constraints.

Metric	Туре	GT 8 pax	GT 65 pax
Design block fuel	Objective	Minimize	
Cumulative LTO noise margin	Constraint	≥5EPNdB	
Takeoff field length	Constraint	≤ 7,000 ft	≤ 11,000 ft
Landing field length	Constraint	≤ 7,000 ft	≤ 11,000 ft
Cutback altitude limit	Constraint	≥ 984 ft	≥ 689 ft
Approach Speed	Constraint	≤ 165 KTAS	
Span	Constraint	≤ 79 ft	≤ 118 ft
Speed below 10,000 ft	Constraint	≤ 250 KTAS	
Cutback Ground Track Dist.	Constraint	≤ 21,325 ft	
Speed increment above V2	Constraint	≥ 10 KCAS	
Speed increment above VO	Constraint	≥ 0 KCAS	
Lift-off speed	Constraint	≤ 205 KTAS	
Cutback 10dB down period	Constraint		
Sideline 10dB down period	Constraint		

To select a design point, JMP's optimization functionality was used. A desirability function was defined for each objective and constraint. In JMP desirability functions are defined as a smooth piece wise function through three points, (2025 JMP Statistical Discovery LLC). An approximately linear increase in desirability was applied for decreasing block fuel, while constraints were model as approximately a step function with values satisfying the constraints being given a desirability of 1, and values which do not satisfy the constraints given a desirability between 0 - 0.01, (with 0.01 being given to values near the constraint value). Initially all solutions which violated the constraints were given a desirability of 0, but it was found that allowing for some desirability gradient in the constraint violating region. JMP used a gradient descent algorithm to optimize for maximum desirability, (2025 JMP Statistical Discovery LLC), and multiple random starts were used by JMP to search for a global optima rather than just a local optima. The solution space proved to be small and it proved to be difficult to find a solution which satisfied all constraints, during intermediate runs, multiple variations of the LTO Noise Margin constraint were tried, such as relaxing this constraint and even changing this from a constraint to an objective with the maximization goal. Once a viable solution space was approach, LTO Noise margin was reset to the 5 EPNdB constraints. Towards the end of the design space exploration Monte Carlo simulations were utilized by running cases around the JMP optimized solutions to see if a more optimal solution could be discovered. All solutions considered for the final selection were rerun in FASST in order to ensure that surrogate error did not result in a viable solution for the optimizer that was unviable once it was simulated in FASST. If needed, additional DoEs were simulated around a design point found by this process and surrogates were recreated for this new data set in order to provide increased granularity around the solution space and to discover a more optimal solution.





Once a design point was selected, studies were done using the selected vehicle design where the engine and vehicle design parameters were frozen, and LTO operational parameters were varied in order to explore how LTO Noise varied with different target values of takeoff reference speed. This approach utilized the same methodology used to select a vehicle design point, but with a more limited set of variables and changing the LTO Noise to be an objective with the goal to maximize that value and changing speed increment above V2 from a constraint to a target so that this Maximum LTO Noise could be determined across a sweep of speeds.

Results

The results in this section pertain to a 65-pax aircraft designed for Mach-1.7 cruise and a range of 4,250 nautical miles and an 8-pax aircraft designed for Mach-1.4 cruise and a range of 4,250 nautical miles. Table 16 shows the selected design point for each of the two vehicles and Table 17 shows the VNRS procedure and LTO Noise performance for each selected vehicle.

Figure 19 and Figure 20 show the sensitivity of these fixed vehicles LTO Noise to various V2+X values. These studied fixed the vehicle shown in Table 16, but reoptimized the VNRS procedures. A Total of 5 different VNRS optimization procedures were examined: The first allowed for all VNRS parameters to be varied; The second allowed for all VNRS parameters besides PLR to be varied and PLR was fixed to 10%; The third allowed for all VNRS parameters besides PLR to be varied and PLR was fixed to 20%; The forth allowed for all VNRS parameters besides PLR to be varied and PLR was fixed to the baseline value shown in Table 17; The fifth allowed for all VNRS parameters besides PLR to be varied and PLR was fixed to 0%. From these studies it can been seen that the 8-pax vehicle had its LTO Noise performance increase with Speed Increment above V2 up to the point where Speed Increment above V2 could not be further increased due to constraint. This held true across all VNRS optimization schemes. Most of this increase came from better flyover noise performance as flyover noise Margin increased with Speed Increment above V2 while lateral noise margin slightly decreased with Speed Increment above V2. The 65-pax vehicle achieved its maximum LTO Noise Margin value with a Speed Increment above V2 between 15 knots and 25 knots with some variation across VNRS optimization schemes. For the 65-pax Flyover Noise Margin generally increased with Speed Increment above V2, while Lateral Noise Margin was mostly level. For both the 8-pax and 65-pax, it can be observed that with increasing levels of PLR, Lateral Noise Margin increased, while Flyover Noise Margin decreased. One of the reasons for this trend is that higher levels of PLR decreased the altitude at which the vehicle could passed over the flyover observer for identical Speed Increment above V2, as the vehicle would require longer to accelerate to the target speed with reduced thrust and would have less time to climb. Another reason for this trend is that higher PLR significantly decreased the throttle setting of the engine for the period where lateral noise was measured, but higher PLR would have a much smaller effect on the throttle setting of the engine for the period where flyover noise would be measured, as the cutback procedure set the throttle setting for the flyover measurement period.





Table 16. Designs of the Georgia Tech SSTs.

	Metric	GT 8 pax	GT 65 pax
Wing	Span [ft]	72	118
	Aspect Ratio	2.82	2.52
	Sweep [*]	55.7	61.6
	Taper Ratio	0.114	0.109
	Thickness-Chord Ratio	0.0335	0.0336
	Fan Pressure Ratio	2.02	2.02
Engine	Overall Pressure Ratio	27.1	27.4
	Bypass Ratio	3.67	3.12
	T41 max [°R]	3,300	3,451
	Top of Climb %N1c	100	97.5
	Rated Thrust [lbf]*	27,292	38,995
ng	T/W	0.399	0.294
Sizing	W/S [psf]	60.9	78.9
	Ramp Weight [lbs]	112,317	435,868
Weights	MTOW [lbs]	111,874	434,530
	MLW [lbs]	67,388	278,383
	OEW [lbs]	59,962	235,703
	Total fuel [lbs]	50,675	186,515
	Block fuel [lbs]	45,176	158,228





 $\textbf{Table 17.} \ \ \textbf{VNRS and LTO Noise performance for the Georgia Tech SSTs.}$

	Metric	GT 8 pax	GT 65 pax
Design Operational Parameters	Takeoff Thrust Derate [%]	0%	0%
	Liftoff Speed [KCAS]	190.6	202.50
	Programmed Lapse Rate [%]	36.3%	29.0%
ational	Spool Rate [%/s]	5.0	2.26%
n Opera	Initial Flight Path Angle [*]	2.5	3.36
Design	Acceleration Time [s]	12.83	20.4
	Cutback distance [ft] Cutback Altitude [ft]	17,011 1,101	20,586 695
Part 25 Field Performance	FAR TOFL [ft]	6,978	10,565
	FAR LDGFL [ft]	4,958	8,020
	Vapp [kts]	125	151.4
Part 36 Takeoff Reference Speed and Noise	Part 36 Takeoff Reference Speed (V2 + X) [KCAS]	173.3 + 46.1	194.1 + 17.1
	Chapter 14 Cumulative Noise (Margin) [EPNdB]	5.65	284.22 (5.14)
	Chapter 14 Lateral Noise (Margin) [EPNdB]	8.88	91.49 (7.92)
	Chapter 14 Flyover Noise (Margin) [EPNdB]	2.56	98.25 (2.88)
Pa	Chapter 14 Approach Noise (Margin) [EPNdB]	2.56	94.48 (8.34)





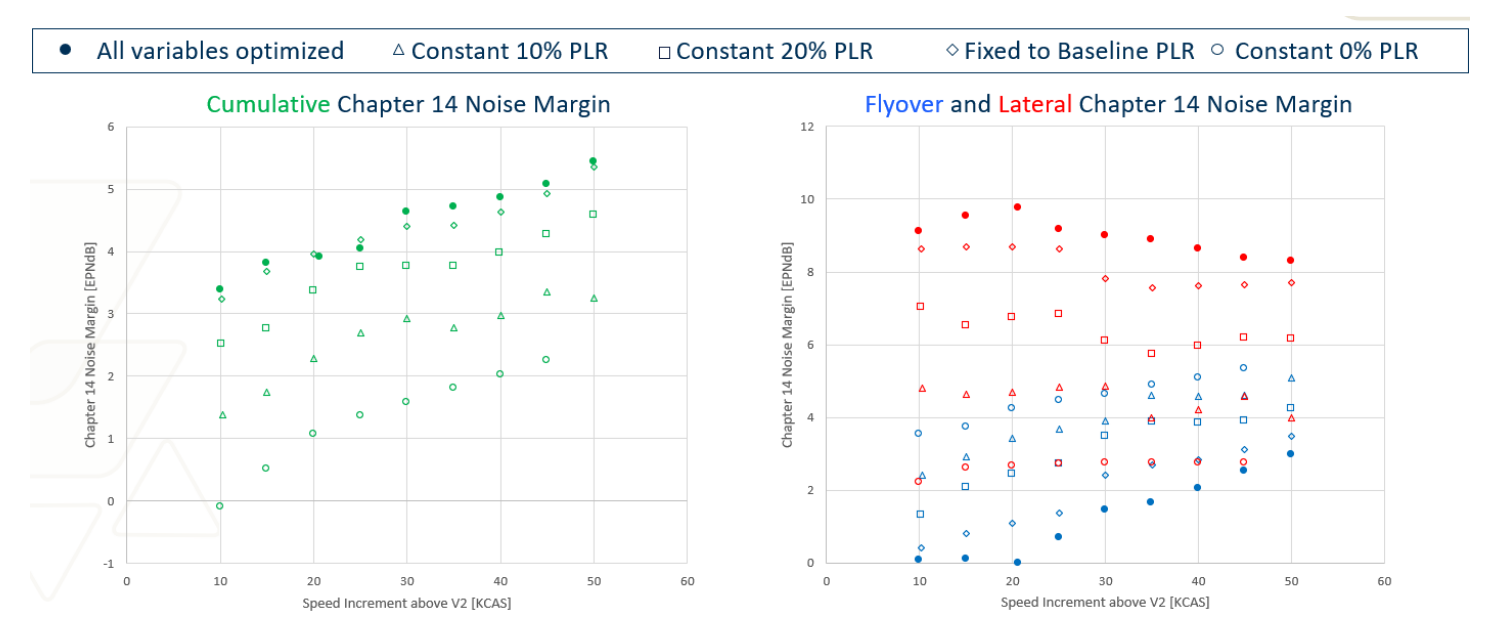


Figure 19. 8pax LTO Noise sensitivity to V2+X under various VNRS Optimization Scenarios.

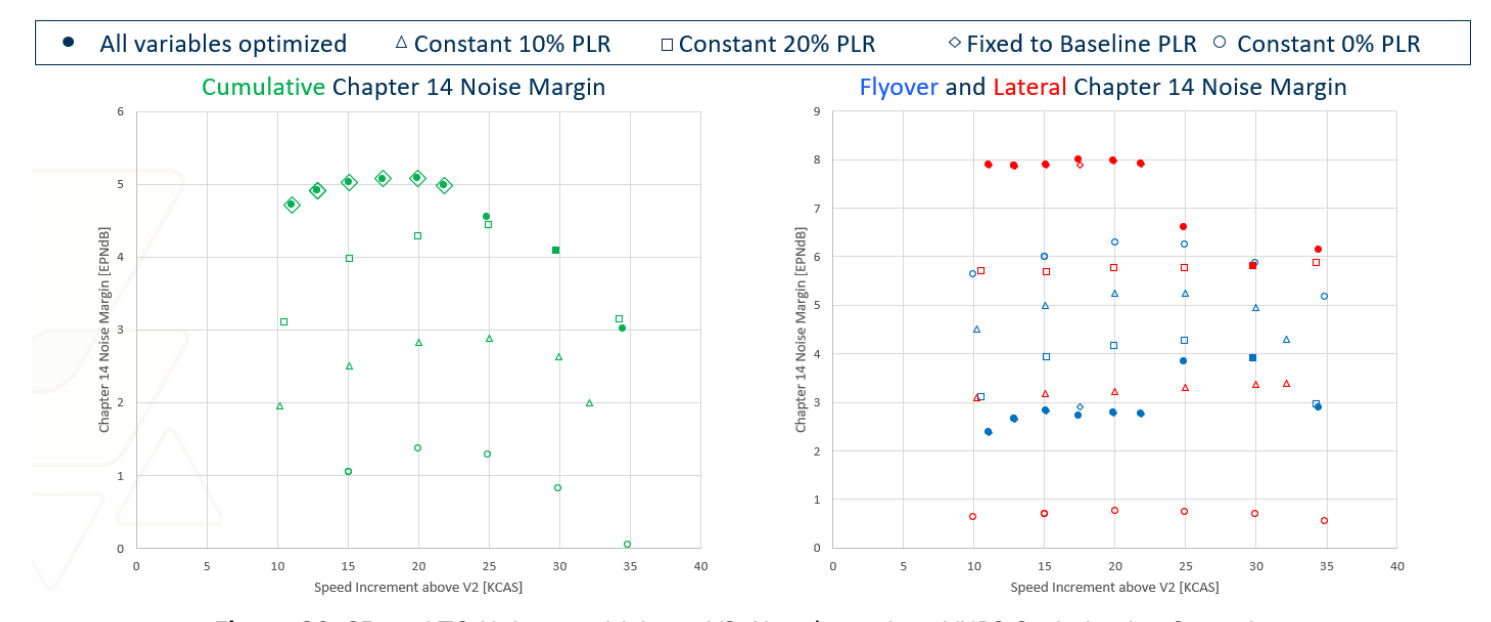


Figure 20. 65pax LTO Noise sensitivity to V2+X under various VNRS Optimization Scenarios.

References

HTCondor (n.d.). Computing with HTCondor. https://research.cs.wisc.edu/htcondor/

Pratt and Whitney and General Electric Aircraft Engines (2005) *Critical Propulsion Components Volume 1: Summary, Introduction, and Propulsion Systems Studies.*

SAS Institute Inc. (n.d.). JMP®, Version 16. https://www.jmp.com/en_us/events/mastering/topics/new-in-jmp16-and-jmp-pro16.html



Tong, M. T., & Naylor, B. A. (2008). An object-oriented computer code for aircraft engine weight estimation. *Proceedings of the ASME Turbo Expo, 1* (December), 1-7. https://doi.org/10.1115/GT2008-50062

Wells, D. P., Horvath, B. L., & McCullers, L. A. (2017). The flight optimization system weights estimation method. NASA/TM-2017-219627

Task 6 - GT Fleet Analysis

Georgia Institute of Technology

Objective(s)

The fleet analysis conducted by Georgia Tech mainly focused on the fuel burn, CO₂ and NO_x emissions for the -developed SST vehicle models. Georgia Tech's Fleet Analysis for prior models developed by this project are described in the A10 2021 Annual Report (Mavris et al., 2021). For the vehicles models described in previous sections of this report, the fleet analysis is performed under NASA University Led Initiative (ULI) titled *Lowering Emissions and Environmental Impact from Civil Supersonic Transport* in 2024 due to ASCENT Project 10 conclusion.

References

Mavris, D., Crossley, W., Tai, J., & DeLaurentis, D. (2021). Project 010 Aircraft Technology Modeling and Assessment. Available at: https://ascent.aero/project/aircraft-technology-modeling-and-assessment/

Task 7 - Purdue Fleet Analysis

Purdue University

Objectives

The Purdue team pursued three subtasks as part of the fleet analysis task. During the prior year, the team created and used the performance and cost coefficient of six additional SST concepts of combinations of passenger capacity and Mach number, implemented a SAF price evolution model, and estimated the effect of SAF utilization in subsonic-only and subsonic and supersonic scenarios. With modifications to FLEET to accommodate these changes, the team estimated the impacts on future environmental emissions when different types of SST concepts were introduced in the fleet and when SAFs were used to reduce the impact of the SST. Purdue completed their work during the 2023 performance period and their final results were published in the A10 2023 Annual Report (Mavris et al., 2023).

References

Mavris, D., Crossley, W., Tai, J., & DeLaurentis, D. (2023). Project 010 Aircraft Technology Modeling and Assessment.

Available at: https://ascent.aero/project/aircraft-technology-modeling-and-assessment/

Outreach Efforts

None

Awards

None

Student Involvement

Student involvement for Purdue team is summarized in A10 2023 Annual Report (Mavris et al., 2023).

The Georgia Tech team also included the following graduate students during this year's effort:

Edan Baltman, Joao De Azevedo, Barbara Sampaio, Jiajie (Terry) Wen, Ted Vlady, Nikhil Iyengar, Zayne Roohi, Srikanth Tindivanam Varadharajan, Carter J. Tegen, and Divya K. Kalaria.

The Georgia Tech team also trained one undergraduate student, Madeleine Graham, in matters related to CFD and optimization, using the 65-pax, Mach-1.7 baseline configuration as a starting point.

